JPCCCK

OCTOBER 27, 2011
VOLUME 115
NUMBER 42

pubs.acs.org/JPCC

THE JOURNAL OF PHYSICAL CHEMISTRY C

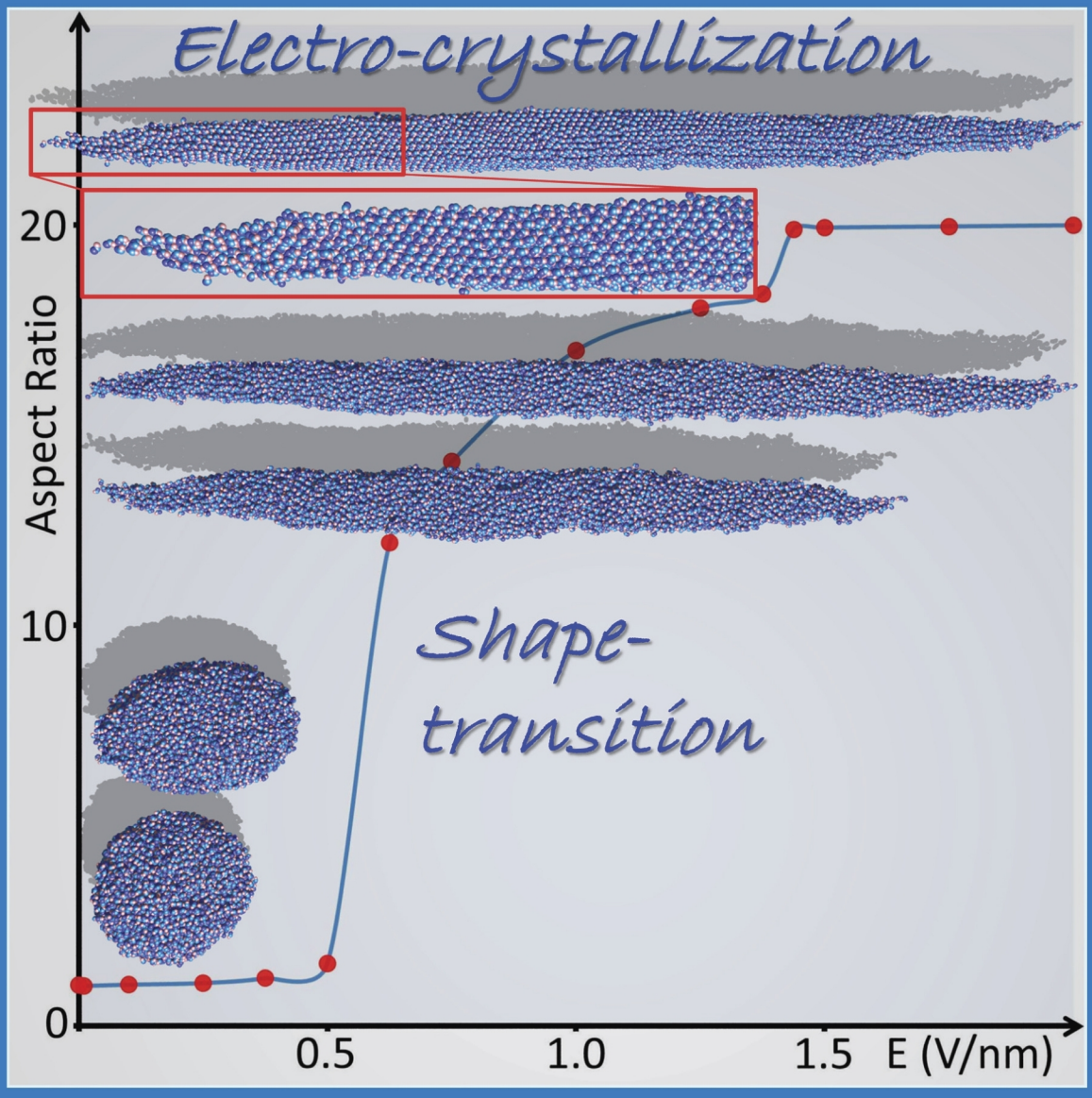

Electric Field-Induced Shape Transformations and Electrocrystallization of a 10 nm Diameter Liquid Formamide Droplet (see page 20343)

NANOMATERIALS, INTERFACES, HARD MATTER

ACS Publications
MOST TRUSTED. MOST CITED. MOST READ.

www.acs.org

THE JOURNAL OF PHYSICAL CHEMISTRY C

FEATURE ARTICLE

pubs.acs.org/JPCC

Dielectric Nanodroplets: Structure, Stability, Thermodynamics, Shape Transitions and Electrocrystallization in Applied Electric Fields

W. D. Luedtke, Jianping Gao, and Uzi Landman*

School of Physics, Georgia Institute of Technology, Atlanta, Georgia 30332-0430, United States

ABSTRACT: The response and properties of a dielectric nanodroplet with a 10 nm diameter made of formamide placed in a uniform electric field are explored with molecular dynamics simulations and an analytic free energy formulation. Increasing fields cause the initially spherical liquid droplet to undergo gradual prolate spheroidal elongation along the field direction that culminates in a shape instability and a first-order shape transition to a slender liquid needle at a field of ∼0.50 V/nm. This transition is accompanied by enhanced reorientation of the molecular dipoles along the field direction, with the elongated droplets exhibiting a field-induced ferroelectric state, unlike the state of the droplet under field-free conditions. For larger fields, we find further gradual enhancement of the molecular dipole reorientation and the onset of a first-order electro-crystallization transition at a field of 1.4375 V/nm. This transition is portrayed by a sharp increase in the positional order parameter, a significant decrease in the molecular diffusion, and further preferential reorientation of the dipoles. Both transitions exhibit hysteresis as the change in the electric field is reversed, that is, for decreasing fields. Data from the molecular dynamics simulation were used for determination of the field-dependent dielectric permittivity of the formamide droplet. An analytic dielectric continuum model is developed, and a free energy expression which includes polarization, surface, and saturation terms is formulated, yielding results for the variation of the droplet shape as a function of the applied field, or electric Bond number, in agreement with the results obtained from the molecular dynamics simulations. Proper inclusion of dielectric saturation effects in the continuum model, expressed in terms of an electric field-dependent dielectric permittivity, is found to play an important role.

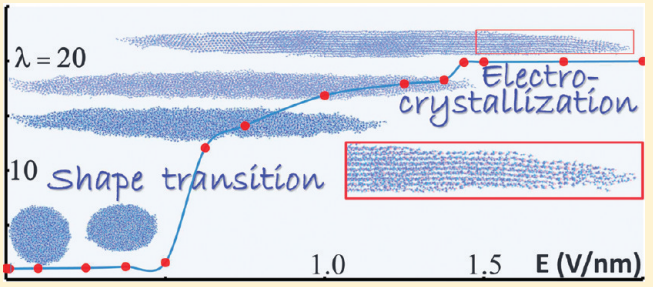

1. INTRODUCTION

The fundamental properties of both neutral and charged liquid drops (nonconducting as well as conducting), under the influence of applied uniform electric fields which may cause shape deformation and possible drop breakup (fragmentation), have been subjects of continued basic and applied research efforts (see reviews in refs 1−12). These systems are of interest in diverse venerable areas including: electrospray ionization,[1,2,7,13] aerosol science,[12] meteorology,[14,15] electrospray propulsion,[2,16,17] inkjet printing,[18] electrospining,[19] nanoencapsulation,[20] and targeted drug delivery.[21] Additionally, there has been significant interest in the properties of liquids as insulating materials under high-voltage conditions because of their high dielectric strength.[22]

Early fundamental observations on the effects of electric fields (and charges) on liquid drops have been made by Lord Rayleigh,[23,24] and shape changes culminating in formation of conical tips occurring for drops held at the end of a capillary have apparently been described first in 1917 by Zeleny.[25] Both Zeleny and later Wilson and Taylor,[26] who explored the response of soap films to applied electric fields, have observed the emission of fine fluid threads from the conical tips, subsequent to shape deformation. A seminal contribution was made in 1964 by Sir Geoffrey Ingram Taylor, who, being primarily interested at the time in the behavior of water drops in strong electric fields (such as in thunderstorms), demonstrated nearly conical equilibrium shapes of water drops at the end of a specially formed electrode.[27] Moreover, and most pertinent to the subject of our investigation, there is the theoretical model advanced by Taylor for the response of the drop to the applied electric field, which was based on an assumed prolate spheroidal shape and a normal-stress balance satisfied at both the poles and the equator of the drop.

The exposure of a drop to an electric field can cause various responses, such as shape deformation, rotation, coalescence, or breakup. In this study, we focus first on field-induced shape deformations of a dielectric droplet. The problem may be stated as follows: a dielectric liquid droplet placed in an electric field will become polarized, and the shape of the droplet will be determined by a balance between the electrical forces on the induced surface charges and the interfacial tension forces. Alternatively, this can be stated as a complex minimization problem where a search should be performed for the shape that yields the lowest total energy (that is, the sum of the electric and surface contributions). The difficulty lies in the interdependence (coupling) of the electric field distribution (as well as the surface tension or

Received: July 13, 2011
Revised: August 26, 2011
Published: September 01, 2011

dx.doi.org/10.1021/jp206673j | J. Phys. Chem. C 2011, 115, 20343–20358

surface energy) and the droplet shape, which must be determined self-consistently. The competition between the electrical and capillary forces (energies) emerges in many areas involving electrohydrodynamic flow. For example, some of the most relevant physics involved in colloid thrusters and electrospray devices operating in the cone-jet mode may be seen already in the simpler problem of an elongated liquid drop in a uniform external electric field, including the formation of electrified jets and emission and acceleration of small charged droplets at the ends of the elongated parent drops. This is a classic problem in the study of electrified fluids that has been studied both experimentally and theoretically,[2,5,7,27−32] and it parallels similar phenomena in ferromagnetic fluid drops under the influence of an externally applied magnetic field.[5,29,32,33]

The desire to identify and understand electric-field-induced properties of liquid droplets on a molecular level, coupled with the possible emergence of new physical behavior in fluid systems with sizes reduced to the nanoscale range (particularly pertaining to the formation and stability of nanoscale fluid structures, e.g., nanojets and nanodroplets),[2,9,34] coupled with the ever-continuing trend of device miniaturization, provide ample motivation for investing research efforts aimed at gaining deeper insights into these issues. In this paper, we focus on theoretical molecular dynamics (MD) simulations and phenomenological investigations of the response to applied static electric fields of a dielectric droplet of nanosclae dimensions (diameter of 10 nm under field-free conditions) made of formamaide ($HCONH_2$). This molecular fluid was chosen because of the high molecular electric dipole moment of formamide (∼3.9 D, that is, about twice that of an H_2O molecule) and the consequent propensity for solvation of salts at relatively high concentrations, thus making it a working material in current experimental, and theoretical, studies of electrosprays, electrified jets, and colloidal thrusters.[2,17,35] We note that formamide has also been the focus of experimental and theoretical studies since it represents a simple model compound displaying the same type of hydrogen bonding between amide groups present in many biological systems.

In our study, the formamide nanodroplet is placed in a constant uniform electric field along a given axis (the z-axis), and the properties of the droplet are probed as the strength of the applied field is varied up to 2 V/nm, which is the range of fields of relevance to current research in areas related to the formation and stability of droplets in electrosprays and colloid thrusters.[2,35] This magnitude of the field is large enough to generate a pronounced elongation of the formamide droplet. We vary the field strengths over a wide range and compare the results obtained from our MD atomistic simulations with those which can be calculated through the use of continuum theories.[5,27,29,30] Our results show that under the influence of fields of about 0.5−1.5 V/nm the droplet exhibits shape changes, transforming from an equilibrium sphere at zero field to a prolate spheroidal shape with field-dependent long axis (c) to short axis (a) aspect ratios, $\lambda = c/a$, of the order of ∼15−20. In these elongated droplets, the molecular dipoles are found to be reoriented by the field along the long axis of the droplet (coinciding with the field direction), thus exhibiting a ferroelectric state (unlike the state of the droplet in field-free conditions).

Furthermore, we find that for larger external electric fields first-order electro-crystallization of the droplet occurs. This leads us to conclude that external electric fields can influence in an essential manner the shape, structure, and thermodynamic (e.g., aggregation phase, that is, transition from liquid to solid) properties of dielectric droplets.

Before we provide a synopsis and the plan of the paper, we comment again on the common occurrence of electric field strengths in the volts/nanometer range in studies of electrified fluid/vacuum interfaces involving charged and dielectric fluids. For example, in electrospray devices the electric fields at the apex of a Taylor cone,[2] where a fine jet is formed, are on the order of volts/nanometer, even though the average field due to the nozzle to extractor potential may be much smaller. This is true as well in the high curvature regions of droplets of dielectric/ionic mixtures, resulting in electric fields that are large enough to cause elongation and possible emission of charged droplets.[2] Even under external field-free conditions, a charged droplet may fission or emit cluster ions when the excess charge is large enough,[36] due to its self-field, and under such circumstances the maximum field at the surface can again be of volts/nanometer magnitude at the regions where much of the interesting and relevant physics takes place, e.g., where instabilities and charged jets emanate and clusters detach.

Following a description of the molecular dynamics simulations (MD) in Section 2, we discuss in Section 3 results of the simulations pertaining to properties (density, melting point, diffusion constant, and surface tension) of field-free liquid formamide which compare well with experimentally measured data. In Section 4 we focus on the electric-field-induced thermodynamic, shape, structural, and other physical properties of the simulated formamide (10 nm diameter) droplet. We start with a presentation of MD results about field-induced shape changes of the droplet, which (starting from a field-free spherical liquid droplet) is found to be described well, as a function of the applied field, as a prolate spheroidal (PS). The elongation process is found to culminate in a shape transition into a needle-shaped liquid droplet with an aspect ratio $\lambda = c/a = 12$, where c and a are the long and short semiaxes of the elongated PS, occurring at a critical value of the applied electric field $E_{0c} = 0.5$ V/nm. In the highly elongated state, the dipoles of the formamide molecules orient preferentially along the applied field direction (the long axis, c, of the PS) exhibiting a high degree of hexagonal order in the (cross-sectional) plane normal to the c axis. The aspect ratio increases gradually for higher fields, culminating in an electrocrystallization (ec) phase transition at $E_{0ec} = 1.4375$ V/nm, where the prolate-spheroidal liquid droplet develops crystalline order with the dipoles showing further orientational ordering along the c axis, and the crystallization transition of the droplet is signaled by a sharp vanishing of the molecular diffusion constant.

A continuum model of the shape elongation and shape transition is developed in Section 5. The model is based on a description of the response of the PS droplet to the applied electric field in terms of a field-dependent dielectric function formulation, which with the inclusion of nonlinear dielectric saturation effects is found to yield a faithful description of the atomic-scale MD simulation results. We also describe in Section 5 a free-energy model for the nonlinear prolate spheroidal dielectric droplet, which compares well with the MD results, and discuss the van der Waals contribution to the droplet's surface and internal potential energies. Finally, we analyze the entropy changes of the droplet as a function of the applied field. In Section 6 we offer a summary of our results.

2. COMPUTATIONAL METHODOLOGY

The principal theoretical methodology that we employ in this study is molecular dynamics (MD) simulations where the equations of motions of the interacting particles are solved numerically

with very high spatial and temporal resolution (typically 0.01 nm and under 0.01 ps). To simulate systems that are large enough, thus allowing assessment of concepts derived on the basis of continuum theories, it is important to utilize simple efficient representations of the interatomic forces. Formamide is a planar molecule whose internal degrees of freedom and intramolecular forces are of much lesser significance for the phenomena explored by us here. Consequently, we treat the formamide molecule as a solid body using quaternion dynamics,[37a] implemented via a midstep implicit leapfrog algorithm[37b] that has been shown to be an extremely stable integration scheme (with only a very small energy drift occurring for long simulation periods). The geometry of the molecule is taken from high-resolution X-ray studies of crystalline formamide.[38]

In our simulations, we employed the AMBER force field parameters[39] for the intermolecular van der Waals interactions between the atomic sites located on different molecules. For the atoms of the formamide molecule, we use the CHELP-BOW[40] partial charges; these have been shown to give a good overall description of the electrostatic potential of the molecules. We remark here that the model does not include field-induced electronic polarization, and consequently, the dielectric response that we explore is due to molecular reorientations caused by the applied field. This approximation is well justified since, using the measured[41] electronic polarizability of formamide ($\alpha = 4.08 \times 10^{-24}$ cm^3), the dipole moment induced ($\mu_{ind} = \alpha$ E) by a field of 1 V/nm is $\mu_{ind} = 0.136$ D, which is merely about 3.5% of the permanent dipole of the formamide molecule (3.9 D) for electric fields of interest in our study. While no truncation is used for the electrostatic (Coulomb) interactions, the weak intermolecular van der Waals interactions are truncated on a group basis through the use of a smooth switching function[42] that depends on the distance between molecular centers of mass so that entire groups of atoms on one molecule interact with the entire group of atoms on another molecule.

Since large-scale atomistic simulations involving electrohydrodynamics of complex fluids are rather scarce, we explored first certain issues pertaining to achieving faithful modeling of such systems. In particular, we interrogated first the employment of long-range Coulomb interatomic potentials with finite interaction cutoffs. Our test studies of formamide droplets in uniform external electric fields of varying strengths have shown the emergence of significant cooperative many-body effects within the dipolar fluid as the cutoffs were increased from values of ~0.9−1.2 nm (typical values in many studies involving atomic partial charges) to 3.6 nm. For example, droplets that maintained their spherical shape when simulated with small interaction cutoffs exhibited significant elongation as the cutoff increased as a result of cooperative dipole−dipole and dipole−field interactions, in qualitative agreement with existing continuum theories of dielectric fluids in electric fields.[5,29,30] From these observations, it became apparent that the long-range interactions needed to be treated more accurately, that is, without the employment of cutoffs.

To address these issues, we implemented a parallel version of the fast multipole method, FMM,[43] adapted for our purposes. In the FMM, a system is spatially represented in a large, roughly cubic, "root-cell". The latter contains a hierarchy, or "tree-structure" division, of "child" subcells obtained by dividing the root-cell into octants and then allowing these child cells to be the parent cells of further binary subdivisions until one reaches the smallest "leaf" cell. Electric multipole moments are computed for all cells at all levels from the atomic charges belonging to molecules contained within the cells. Atoms belonging to molecules in the basic leaf cell interact directly with all the atoms of molecules in neighboring leaf cells, while they interact only with the multipole moments of more remote cells; the more remote the cells are from the central leaf cell, the larger the cells are allowed to be. Thus, an atom interacts with a small set of multipoles representing entire, increasingly larger, volumes of remote space, rather than with all of the atoms contained within it—this is the main feature that enables one to model efficiently large systems involving long-range interactions. We carried the multipole calculations to $m = 6$ ($m = 0$ and 1 are the monopole and dipole levels). The size of the smallest (leaf) cell was 1.2 nm, and this value was used as the spherical cutoff for the short-range van der Waals interactions.

For the simulations performed at constant temperature, we use a velocity rescaling algorithm[44] (see also ref 37, eq 7.59) with a relaxation time of 3 ps. This is applied only to the molecular center of mass velocities. We have observed that equipartition of energy between translational and rotational degrees of freedom is very rapid, and there is no need to directly modify the rotational kinetic energies. Additional details of our code necessary for this study will be described further as we discuss our results.

3. PROPERTIES OF THE FIELD-FREE LIQUID

To assess the merits of the parametrized interaction potentials used in our simulations, we tested first certain thermodynamic and physical properties of the simulated formamide model, including evaluations of the melting point, surface tension, and diffusion constant. Since experiments on liquid formamide are commonly performed around room temperature (that is about 25 K above the melting point of crystalline formamide), we focus here on results obtained from MD simulations performed at this temperature range. As shown below, the results of these exploratory simulations validate in a quantitative way the accurate description of the thermodynamic, structural, and transport (diffusion) properties of the formamide model, in both the solid and liquid phases and at phase coexistence.

Melting Point, Density, Diffusion Constant, And Surface Tension. The melting point of the modeled liquid formamide was estimated as the coexistence temperature of the crystalline and liquid phases. A crystalline slab containing ~5200 molecules was constructed according to the crystallographically determined $P2_1n$ space group structure[45] with the crystalline layers (formamide sheets) lying parallel to the xy plane, with two free surfaces (vacuum interfaces) along the z-axis. Two-dimensional periodic boundary conditions (2D pbcs) were imposed in the xy plane, and reflecting boundary conditions (in the z direction) were employed, acting on any gas-phase molecule encountered at the ends of the computational cell. In these simulations, we replicated the basic root-cell (including its tree structure) and "stacked" three of them along the z-axis to create a long narrow tree structure (requiring an appropriately modified nonstandard FMM algorithm;[2] this formulation is particularly useful for efficient simulations of systems such as highly elongated droplets or long liquid jets). The size of each FMM root-cell was ~5.8 nm (in the x direction), 4.7 nm (in y), and by 5.6 nm (in z) giving a z-dimension of the calculational cell of ~3 × 5.6 nm, while the solid slab (centered about $z = 0$) extended about 11 nm along the z-axis, leaving ~3 nm of free space at each end of the computational cell.

After equilibrating the system well below the experimental melting point, the energy of the system was elevated via scaling of

the particles' velocities with subsequent lengthy constant energy equilibrations, until approximately a third (along the z-axis) of the system was melted and continued to evolve in equilibrium with the remaining solid part; for a description of the simulation method used for determination of the melting point, see ref 46a. The temperature corresponding to this liquid/solid coexistence state, i.e., the melting point, was found to be close to 285 K, which is 9 K above the experimental value[46b] of 276 K. Accordingly, to ensure that the simulated system is well into the temperature range corresponding to a liquid phase, we chose to perform our simulations at T = 310 K (that is, shifted by 10 K above room temperature, T = 300 K); this shift does not affect the physical behavior of our system in any noticeable manner. The density of the simulated formamide crystal was found to be 1.26 g/cm^3 in agreement with the experimental value[45a] (1.26 g/cm^3).

The density and diffusion constant of liquid formamide were determined by us from constant (zero) pressure simulations of bulk liquid formamide, where the spatial dimensions of a cubical root-cell were allowed to vary, while using 3D pbc and the FMM with a modified constant-pressure algorithm.[37,44] We have also modified the FMM algorithm so that when periodic boundary conditions are employed the tree structure of the root-cell, along with all its computed multipoles, is replicated as neighboring image cells. In this way atoms in the central computational cell are acted on by the correct multipole structure as they interact with all of their neighboring periodic image cells. The width of the cubical root cell was ∼6 nm. The density of the pure formamide liquid (at 310 K) was found to be ∼1.10 g/cm^3 in good agreement with the experimental value[46b] of 1.13 g/cm^3, and the computed diffusion constant was found to be $\sim 1.2 \times 10^{-5}$ cm^2/s which compares well with values ranging from 0.55 to 1.27 $\times$ 10^{-5} cm^2/s estimated from previous experiments and simulations.[47]

Since capillary forces act as a major driving force in the phenomena that we study, it is important to obtain an estimate for the surface tension of the simulated liquid. To this aim, we determined the surface tension of liquid formamide in two different ways. First, we simulated a liquid slab maintained at T = 310 K with the same number of molecules and type of boundary conditions as in the liquid−solid coexistence study described above. In this case, we replicate the basic root-cell three times along the z-axis. The width of each cubical FMM root-cell was ∼5.6 nm, giving a z-dimension of the calculational cell of $3 \times 5.6 \sim 17$ nm, while the liquid slab (centered about $z = 0$) occupied ∼11 nm along the z-axis, leaving sufficient space to establish both liquid and vapor regions.

The normal (P_N) and tangential (P_T) components of the molecular pressure tensors were used to find the surface tension γ by integrating the difference ($P_N - P_T$) across each liquid interface.[48] The value that we found, γ = 0.046 N/m, compares well with the experimentally determined value[45] of γ_{exp} = 0.057.

In an alternative method, we used the fact (Young−Laplace relation) that the pressure inside a spherical droplet of radius R is $P = 2\gamma/R$. We formed a spherical droplet of formamide by "carving out" a ∼10 nm diameter drop from the bulk constant-pressure simulation system that we described earlier and allowed it to equilibrate further using "absorbing" boundary conditions; namely, the pbc's were lifted, and the few evaporating molecules that crossed the boundaries of the 19.2 nm wide FMM root cell were removed from the system. Using the averaged hydrostatic pressure in the interior of the droplet and the droplet's equimolar radius, we computed a value of γ = 0.046 N/m in agreement with the value we determined above. The density in the interior of the droplet interior was found to be about 1.11 g/cm^3; results obtained from simulations of a larger diameter droplet (20 nm) agree well with these values.

4. FIELD-INDUCED SHAPE AND CRYSTALLIZATION TRANSITIONS

In this section, we focus on the thermodynamic and electric-field induced structural transformations of the dielectric nanodroplet, with the strength of the externally applied electric field serving as a control parameter. Our investigations were carried out at T = 310 K (see earlier discussion) and involved a droplet with a diameter of 10 nm (under field-free conditions); the droplet contains 7150 formamide molecules (that is, $6 \times 7150 \sim$ 43 000 atoms carrying partial charges). The properties of the drop as a function of the strength of the applied electric field E_0 (from 0 to 3 V/nm) were determined from simulations where for each successively incremented value of the field the drop was fully equilibrated before equilibrium-averaged results were computed.

Prior to presentation of our results, we remark on certain aspects of the analysis of the MD simulations. Shape deformations of the liquid droplet induced by uniform external electric fields leading to the appearance of structures with geometries close to prolate spheroids have been described experimentally and theoretically (using continuum approaches[29,30]). Furthermore, under certain circumstances the emergence of conical regions near the ends of the elongated structures has been observed. In the present study, we have found that the shape of a 10 nm formamide drop placed in a uniform electric field may indeed be well characterized as a prolate spheroid (with the aspect ratio $\lambda = c/a$ between the semimajor (c, long) and semiminor (a, short) axes, varying as a function of the field strength), with some deviation occurring for sufficiently strong fields (i.e., for highly elongated spheroidal shapes) near the ends. A prolate spheroid (ellipsoid) is described in cylindrical coordinates by the equation $(r_z/a)^2 + (z/c)^2 = 1$ (where r_z is the radius at the position z along the symmetry axis), and plots of r_z^2 vs z^2 from our simulation data exhibit a highly linear relationship; the minor and major axes and the corresponding aspect ratios, λ, are determined from least-squares fits to the above equation for different values of the applied field.

In finding the axial profile (r_z vs z), the z-axis (along which the external electric field is applied and the droplet elongates) is divided into bins of width dz = 0.2 nm, and the number of molecules N_z in each bin is computed. Using the mean density, ρ, inside the droplet, an equimolar radius r_z is computed for each z-bin with the relation $\rho\pi r_z^2 dz = N_z$. Additionally, for the chosen bin width dz, one can determine a cutoff radius r_c that corresponds to one molecule, N_z = 1. Starting from the center of the droplet, the first bins along the positive and negative z-axis that have an equimolar radius $r_z < r_c$ are taken as the two end points of the droplet. In performing the least-squares fit of the averaged radial profile data to a prolate spheroid, contributions are included only from bins bracketed between these end points. This procedure yields prolate spheroid shapes consistent with the droplet profiles for both small and large elongations.

The density ρ inside a droplet is determined for each field strength by time averaging the density inside a test volume located in the interior of the droplet whose shape is taken to be the same as that of the droplet itself. This is accomplished by making first a rough estimate of the semiminor and semimajor axes using radial as well as axial binning of the atomic positions

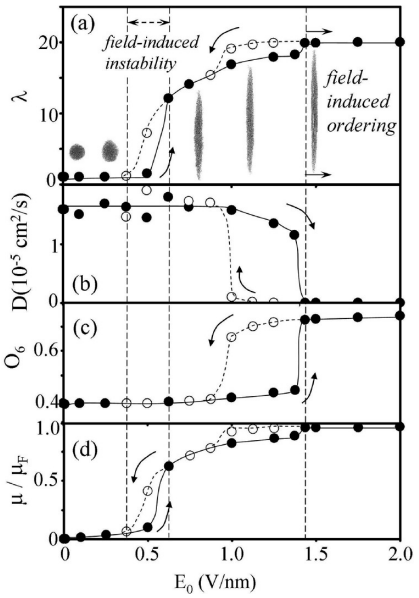

Figure 1. Time-averaged results for properties of the formamide nanodroplet, obtained from MD simulations, plotted as a function of the applied electric field, E_0. Results are shown for both increasing (filled symbols) and decreasing (empty symbols) applied electric fields. (a) Aspect ratio, $\lambda = c/a$, where c and a are the long and short semiaxes of the prolate-spheroidal droplet. Note the sharp increase of λ at $E_0 \sim 0.5$ V/nm, reflecting an elongation shape transition, and the crystallization, ordering, transition at $E_0 \sim 1.44$ V/nm which is signaled by a smaller increase of λ. Both transitions show hysteretic behavior when the field is lowered. Also included are images (side views) of the droplet at various stages of the field-induced elongation and crystallization processes. (b) Diffusion constant of the formamide molecules (center of mass), showing that the droplet remains in the liquid state when it undergoes the shape transition for E_0 near 0.5 V/nm, and a sharp decrease in the molecular diffusion accompanying the crystallization transition. Note the delayed remelting of the crystallized droplet (occurring at $E_0 \sim 1$ V/nm) when the applied field is lowered. (c) The O_6 order parameter showing a sharp increase upon droplet crystallization and an equally sharp decrease upon remelting. (d) z-component of the droplet electric dipole moment per molecule, μ, averaged over all the molecules and normalized by the value of the dipole moment of a formamide molecule, μ/μ_F, exhibiting, as a function of the applied electric field, variations similar to those of the aspect ratio (shown in (a)).

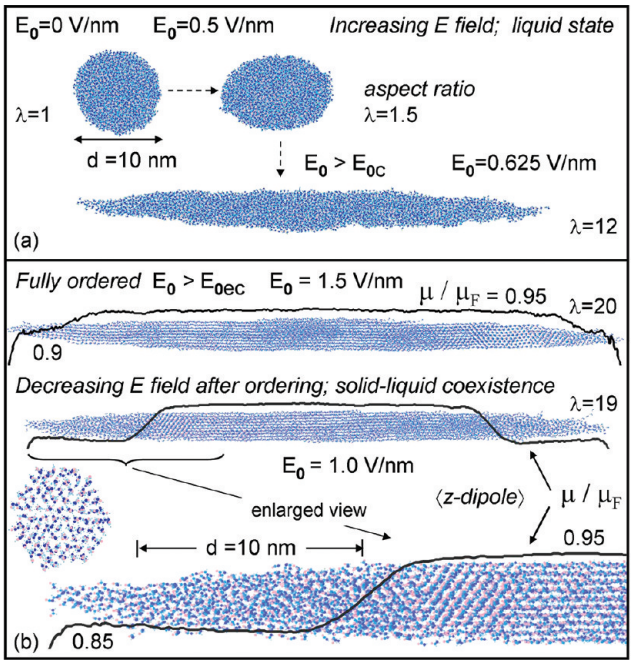

Figure 2. Images of molecular configurations recorded in the molecular dynamics simulations illustrating the progression of stable states of the formamide droplet as the externally applied electric field strength, E_0, is initially raised [images shown in (a) and the topmost image shown in (b) for $\lambda = 20$] and subsequently reduced [shown in (b) for $\lambda = 19$]. The 10 nm length scale shown in (a) applies to all images except the enlarged views (b, bottom). (a) At zero field, the spherical droplet is undistorted with an aspect ratio $\lambda = 1$ which increases to $\lambda = 1.5$ at $E_0 = 0.5$ V/nm with the droplet undergoing a prolate spheroidal distortion. As the field is raised above the critical field, $E_{0c} = 0.50$ V/nm, the liquid droplet undergoes a shape transition by elongating abruptly to an aspect ratio of $\lambda = 12$. A side view of the elongated liquid droplet at a field of 0.625 V/nm is shown at the bottom of (a). (b) When the electric field strength reaches the electro-crystallization critical field, $E_{0ec} = 1.4375$ V/nm, the droplet crystallizes, with further increase in the field causing only a slight change. Shown at the top of (b) is a side view of the fully (electro) crystallized droplet for $\lambda = 20$. As the field is lowered (see Figure 1) the droplet displays hysteretic behavior (b, middle) and exhibits a solid/liquid (sl) coexistence, until a lower field of 1.0 V/nm is reached at which point the system returns completely to the liquid state (see Figure 1). A side view of the droplet showing sl coexistence, with $\lambda = 19$, is shown in the middle of (b). A detailed view of one end of the sl droplet is shown at the bottom, with a 2.5 times enlargement. In the sl coexistence state, lattice planes displaying two crystalline domains differing by a 30° rotation about the c-axis (along the applied field direction) are observed. Also shown is a 2 nm wide cross-sectional view (image at the bottom left of (b)) of an ordered region (enlarged an additional 1.25 times) that is typical of both the fully ordered and sl droplet states. Overlaid on the images of the droplets in (b) is a curve showing the variation of the average z-component of the droplet's electric dipole moment (per molecule), normalized by the dipole moment of a formamide molecule, $\bar{\mu} = \mu/\mu_F$. For both the fully crystalline ordered ($\lambda = 20$) droplet (top of (b)) and the ordered regions of the droplet in the sl coexistence state (see central segment of the $\lambda = 19$ state, middle of (b)), we find $\bar{\mu} = 0.95$; for the former $\bar{\mu} = 0.9$ near the tip, while for the sl coexistence droplet $\bar{\mu} = 0.85$ in the disordered tip region (see bottom image in (b)). In the molecular configurations, the oxygen atoms of the formamide molecule are shown in pink, the hydrogen atoms in light blue, the carbons in light green, and the nitrogens in dark blue.

and determining the largest nonempty radial and axial bins, respectively. The internal prolate spheroid test volume is defined by scaling the so determined lengths of the axes by 3/4; this procedure essentially alleviates uncertainties due to surface effects. The result is not sensitive to the scale factor (3/4) that we employed here; scaling the original axis estimates by 1/2 gives essentially the same density.

Instability, Elongation, Ordering, and Electrocrystallization. The effect of the external electric field is reflected in geometrical, structural, and dynamical properties of the droplet, displayed in Figure 1, where we show the variation with the applied field of the aspect ration $\lambda = c/a$, the molecular diffusion constant D, the normalized dipole moment (per molecule) of the droplet in the field direction (z), $\bar{\mu} = \mu/\mu_F$ (where μ_F is the dipole moment of a formamide molecule), and the order parameter[49] $O_6 = < |\Sigma_{j\subset nn} \exp(i6\theta_j)|/6 >_k$ expressing the degree of hexagonal order in the droplet (with z as the symmetry axis), given by the above average over all the molecules in the droplet, $1 \le k \le N$ (and if desired over a certain simulation interval). To evaluate O_6 we determine first the six nearest-neighboring (nn) molecules

dx.doi.org/10.1021/jp206673j | J. Phys. Chem. C 2011, 115, 20343–20358

($1 \le j \le 6$) to molecule k. The six molecules that are nn to a chosen molecule k are taken to be laterally located with respect to the chosen molecule if they are distanced from it along the z-axis by no more than 0.4 nm and by no more than 0.6 nm laterally (molecules near the surface of the droplet that may have less than six nn are also included). The center of mass (com) positions of nn molecules obeying the above conditions are projected on the xy plane (i.e., the plane normal to the z axis) that contains the com of the chosen (k) molecule. In the above expression for O_6, θ_j is the angle made by the vector (in the xy plane) connecting the center-of-mass of molecule k and the projected com location for molecule j, with an (arbitrarily chosen and fixed for all the molecules) reference axis lying in the xy plane; for perfect hexagonal order of the centers of masses of the molecules, $O_6 = 1$.

Also included in Figure 1a are snapshots of the droplet for selected values of the electric field. Selected representative configurations of the droplet, and some of their associated physical characteristics, taken for various values of the applied electric field, are displayed in Figure 2. Certain distinct features and patterns are evident from inspection of Figure 1, including field-induced shape elongation, ordering, and electric-field-induced crystallization (or electro-crystallization (ec)) that is found to occur for stronger fields. Additionally, we observed pronounced hysteresis when the magnitude of the applied field is decreased.

For fields up to 0.5 V/nm, the liquid droplet elongates mildly in the direction of the applied field. However, for higher fields, the droplet becomes metastable, undergoing an elongation shape transition for applied fields between $E_0 = 0.5$ and 0.625 V/nm. This transition is portrayed by a rapid change in the aspect ratio, λ, which increases in the above range from an initial value of 1.5 to 12 (see Figure 1a), resulting in a needle-shaped droplet (see Figure 2a). The shape transition is accompanied by a marked increase in the normalized z-component of the average molecular dipole moments from about 0.1 to 0.7 (Figure 1d). The field-induced reorientation of the molecular dipoles transforms the droplet to a ferroelectric state, unlike the state of the droplet under field-free conditions where it does not have a net dipole. Throughout the elongation transition (with gradual elongation continuing past the shape transition, for fields in the range of 0.625 V/nm < E_0 < 1.4375 V/nm), the droplet remains liquid (see, respectively, the diffusion constant D and the order parameter O_6 in Figure 1b and 1c for E_0 < 1.4375 V/nm). We note here the gradually diminished molecular diffusivity for fields in the range of 1 and 1.4375 V/nm and the sharp drop to zero associated with electro-crystallization when the field strength exceeds E_{0ec} = 1.4375 V/nm.

The onset of shape instability of dielectric droplets for electric fields exceeding a critical strength has been the subject of earlier studies.[6,27] Indeed, as noted already in Section 1, Taylor predicted theoretically[27] that a droplet of initial radius R (under field-free conditions) will undergo an instability for an external field strength E_0 satisfying (MKS units) $E_{0c}(4\pi\varepsilon_0 R/\gamma)^{(1/2)} = 1.625$. Using for the computed surface tension of the droplet studied here $\gamma = 0.046$ N/m and $R = 4.84$ nm for the computed equimolar radius yields (from the above relation) a predicted critical field $E_{0c} = 0.48$ V/nm, which is only slightly lower than the field found in our simulation at the onset of instability leading to the shape transition (see Figure 1a); when the experimental surface tension $\gamma = 0.057$ N/m is used in the above relation, the predicted critical field strength is 0.53 V/nm.

At a field E_{0ec} = 1.4375 V/nm, a second critical field is reached, signaled by a small, but discontinuous, change in shape, a further elongation to $\lambda \approx 20$, and an increase in $\bar{\mu}$ (see Figure 1 and top configuration in Figure 2b); note the needle-shaped droplet with $\lambda \approx 20$ (calculated for E_0 = 1.5 V/nm) shown at the top of Figure 2b, exhibiting a nonuniform distribution of the (normalized) dipole moment ($\bar{\mu} = \mu/\mu_F$), with the lower values found at the droplet's ends reflecting a somewhat reduced degree of dipolar alignment at these regions. This transition is signaled (unlike the shape change at lower fields, discussed above) by a precipitous increase in the hexagonal order in the droplet (see Figure 1c) and a concomitant discontinuous vanishing of the molecular diffusion in the droplet (see Figure 1b). These changes are the result of a field-induced electro-crystallization (ec) phase transition occurring at E_{0ec}. No further essential changes occur for higher fields $E_0 > E_{0ec}$.

When the strength of the electric field is lowered from that of the electro-crystallized state, the system exhibits a hysteretic behavior. Two transition regimes are found. The first occurs near 1 V/nm. As the field strength is lowered from ~1.44 to 1.0 V/nm (where the droplet was previously in a liquid state), a solid/liquid (sl) coexistence emerges; see middle and bottom configurations displayed in Figure 2b (calculated for E_0 = 1.0 V/nm during the field lowering process) where the middle region of the droplet is characterized by crystalline order, while the regions closer to the ends of the droplet exhibit liquid-like behavior. As the field is decreased from ~1.44 to 1 V/nm, the crystalline middle region gradually reduces in size (compare configurations shown at the top and middle of Figure 2b), and when $E_0 = E_{0sl} \sim 0.8$ V/nm, a transition to a complete liquid state is encountered, where the diffusivity (Figure 1b) and the degree of hexagonal order (Figure 1c) are found to attain liquid-like behavior, while the elongation (λ, see Figure 1a) and z-dipole order parameters (Figure 1d) correspond to an elongated and molecularly aligned (relatively high $\bar{\mu}$) droplet. Generally, we conclude that the trends observed during the solid/liquid coexistence stage are essentially the reverse of those seen when the liquid droplet approaches the electro-crystallization transition from lower fields.

The second hysteretic feature occurs for the liquid-like droplet that, as aforementioned, maintains an elongated and molecularly aligned state (characterized by relatively high values of λ and $\bar{\mu}$) until E_0 = 0.375 V/nm (see Figure 1a and 1d). This type of hysteresis has been addressed in a number of studies.[5,29]

We conclude this section with observations made from both constant-temperature and constant-energy simulations pertaining to the state of the droplet after switching-off (suddenly) the electric field, starting from a highly ordered state (e.g., E_0 =3 V/nm). In both simulations we found that the temporal evolution for return of the droplet to the original spherical liquid disordered state is exponential with a time constant of ~200 ps. In the constant-energy simulation, the temperature of the droplet decreases (since in the recovery process the potential energy increases, i.e., becomes less negative) from its initial 310 to 283 K (which is essentially the same as the bulk freezing point of 285 K determined by us for the simulated fluid, see discussion above).

We have also noted that the state of the droplet at high field strength can be ordered or disordered depending on the temperature. This reflects an interplay between temperature and applied field strength in determining the phase behavior of the dielectric droplet. Taking the polar fluid to a state-saturated polarization under high electric field strength is analogous to the "poling" process used to align dipolar domains in ferroelectric materials,[50] in which a high dc electric field is applied to a sample at an elevated temperature, and after the domains are sufficiently

aligned the temperature is lowered back to room temperature (in the presence of the field) to "lock in" the highly aligned state. This analogy suggests variations of our study in which the temperature of an ordered polarized droplet at high field strength is lowered significantly to explore to what extent the polarization and order can be maintained (locked in) and what behavior will be observed under variations of the applied field.

5. COMPARISON TO CONTINUUM THEORY

The energetics and response of a dielectric droplet in a uniform external electric field have been the subject of a number of theoretical studies.[5,6,29,30] The droplet shape is usually taken to be axisymmetric, similar to the experimentally observed shapes, and the geometry is further refined through minimization of formulated free-energy models via droplet shape variation as a function of the applied external electric field.[29,51,52] There have also been reports about studies based on a force balance approach, where the balance between the electrical and capillary stresses across the droplet surface is considered;[5,6,27,29−31] in some of these approaches, nonlinear polarization effects have been considered.[31] The droplet surface is often modeled as a prolate (elongated) spheroid, PS, which captures the basic overall shape of a droplet undergoing elongation in an electric field. More complex droplet shapes, such as conical droplet ends that can form under certain circumstances, were considered in more detailed studies (see ref 5 for review).

The wealth of detailed information generated in our MD simulations allows us to explore and assess the appropriateness of continuum-based models for the description of the behavior of nanoscale droplets. Such evaluation led us to introduce a new free-energy model in which the shape of the dielectric droplet is represented as a prolate spheroid, but unlike previous models where the permittivity (dielectric constant) is taken to be independent of the field strength, we found that a proper description of the behavior of the droplet requires that the permittivity of the droplet be allowed to vary as a function of the electric field inside the droplet. This leads to the inclusion of a new term in the expression for the free energy. We will show that these modifications to the standard PS free-energy model bring the results of the model into excellent agreement with our atomistic MD simulations. Since the novel aspects of our model are associated with nonlinear dielectric properties, we will refer to our model as the nonlinear prolate spheroid, or NLPS, model.

A. Dielectric Droplets in Strong Electric Fields. When a fluid droplet made up of polar molecules is subject to an external electric field, the resulting field inside the droplet causes both an induced polarization of the molecular charge and a polarization due to dipole orientation. For small field strengths, the polarization (dipole moment, P, per unit volume, V) varies linearly with the internal field strength E, $\mathscr{P} = P/V = \varepsilon_0(\varepsilon - 1)E$, where ε is the relative permittivity (which we sometimes term "dielectric constant", although it is allowed to vary as a function of the electric field[51,52]); we note that MKS units are used here, bringing a scaling factor of $4\pi\varepsilon_0$ compared to the Gaussian units employed in some previous studies. For larger applied fields, the competition between thermal and polarization effects leads to a nonlinear relation between the polarization and the field

$$\mathscr{P} = P/V = \varepsilon_0(\varepsilon(E) - 1)E \tag{5.1}$$

Often, the field-dependent permittivity $\varepsilon(E)$ continues to be referred to as the dielectric "constant". For reference, we remark here that the study of nonlinear dielectric saturation effects, and in particular the response of polar fluids to high field strengths, has a long history, and it remains an active research area.[31,53−56]

In modeling the droplet surface as that of a prolate spheroid, the assumption is normally made that the volume of the droplet remains constant as the droplet undergoes elongation, namely, $V = (4\pi/3)a^2c = (4\pi/3)R^3$ where c and a are the semimajor and semiminor axes of the PS and R is the radius of the initial spherical droplet when under field-free conditions. The symmetry axis of the ellipsoid is taken as the z-axis, and unless otherwise stated, the field and dipole components discussed below are understood to be the z-component. Denoting the droplet's aspect ratio as $\lambda = c/a$, the eccentricity, e, is given by $e^2 = 1 - 1/\lambda$; the eccentricity $e = 0$ for a spherical droplet, and e approaches 1 in the limit of an extremely thin (one-dimensional), elongated droplet. We assume that the droplet is surrounded by vacuum (i.e., dielectric constant of unity).

As aforementioned, an important point of departure of this work from previous investigations is that the dielectric constant of the fluid droplet is taken as a material-dependent quantity that is a function $\varepsilon(E)$ of the internal electric field strength E inside the fluid. The field strength E (understood to be along the z-axis) inside a prolate spheroid subject to a uniform parallel external field E_0 is the sum of the applied field, E_0, and the opposing field created by the induced polarization charges

$$E = E_0 - (P/V)n(\lambda)/\varepsilon_0 \tag{5.2}$$

where P is the total dipole moment of the ellipsoid along the z-axis and $n(\lambda)$ is the z-component of the depolarizing factor.[51,52] $n(\lambda)$ is a function of the eccentricity, $e(\lambda)$, and therefore the aspect ratio λ, through the implicit relation $n(\lambda) = (1 - e^2)\{\ln[(1 + e)/(1 - e)] - 2e\}/(2e^3)$. The two relations (eqs 5.1 and 5.2) give

$$E_0 = [1 + (\varepsilon(E) - 1)n(\lambda)]E \tag{5.3a}$$

and

$$P = \varepsilon_0 V(\varepsilon(E) - 1)E_0/\{1 + (\varepsilon(E) - 1)n(\lambda)\} \tag{5.3b}$$

We note that eq 5.3b, along with the definitions in the preceding paragraph, enables one to compute, using data from the MD simulation, the field-dependent dielectric constant $\varepsilon(E)$ for a droplet having an interior field E (with an external field E_0). For a given imposed external field strength, E_0, the simulations allow us to obtain time-averaged values for the dipole moment of the droplet (P), the semimajor and semiminor axes (c and a), aspect ratio (λ), associated droplet volume V, eccentricity (e), and depolarizing factor, $n(\lambda)$. These values are then used with eq 5.3b to obtain the dielectric constant $\varepsilon(E)$ as a function of both E and E_0; E may be computed using eq 5.2.

The dielectric permittivity as a function of the external field strength, E_0, computed from eq 5.3b (with the use of data obtained from the MD simulations), is shown in Figure 3 (symbols). The observed general monotonic decrease of the dielectric constant for increasing field strengths is consistent with experimental results for various liquids subjected to field strengths similar to those used in our simulations.[54,55] The different symbols in Figure 3 give information on the manner in which (the field-dependent) dielectric constants were computed. The filled symbols in Figure 3 correspond to MD equilibrations in which E_0 (constant for each run) was increased from the field of a preceding equilibration; namely, the configuration at the end of a long equilibration performed at a lower external field serves as the

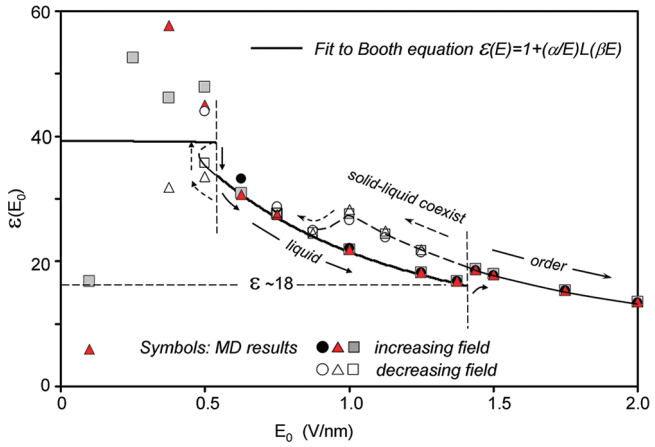

Figure 3. Variation of the dielectric constant with the externally applied electric field strength E_0. The symbols represent values obtained from MD simulations, with solid ones corresponding to increasing values of the applied field, and open symbols obtained from simulations with decreasing field values. The thick dark curve (between the two vertical dashed marker lines) corresponds to the liquid droplet (that is, up to the crystallization (ordering) transition), and it was obtained from a fit of $\varepsilon(E)$ to the generalized Booth equation (eq 5.4 with $s_1 = 0.947$ and $s_2 = 1.117$); it is used later on in the NLPS free-energy minimization. We note the transition to an ordered droplet when $E_0 \sim 1.4$ V/nm (and $\varepsilon \sim 18$) and a pronounced hysteresis as the field is decreased after the droplet has ordered. Note the predicted metastable region occurring for E_0 field values in the range ~0.5−0.6 V/nm.

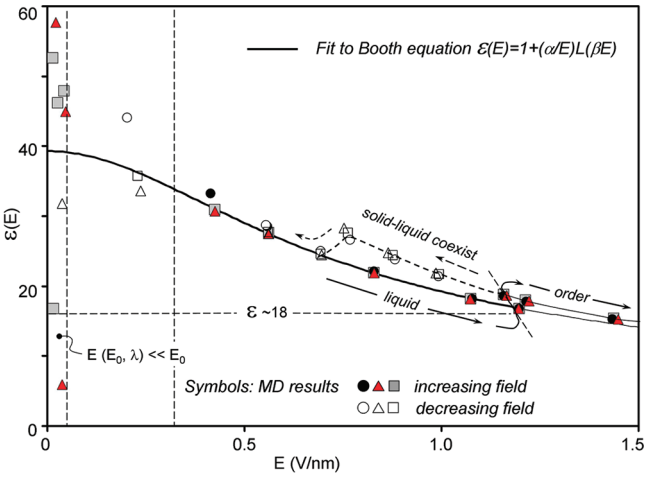

Figure 4. Variation of the dielectric constant with the electric field E inside the droplet. Note the transition to an ordered droplet when $E \sim 1.2$ V/nm (and $\varepsilon \sim 18$) and a pronounced hysteresis as the field is decreased after the droplet has ordered. The thick dark curve derives from a fit of MD data to the generalized Booth (eq 5.4 with $s_1 = 0.947$ and $s_2 = 1.117$). Symbols denote values obtained from the MD simulations, with closed and open ones corresponding to increasing and decreasing applied external field.

starting point for a subsequent simulation performed for an incremented (increased) value of the applied field. The empty symbols correspond to the reverse process where the end configuration from a simulation performed for a given value of the applied field, serves as the starting one for a subsequent simulation at a lower value of the field; comparison between the curves corresponding to the filled and empty symbols allows us to explore hysteretic effects. The circles in Figure 3 are associated with the use (in eq 5.3b) of the total dipole moment, P, and volume, V, of the prolate spheroid (for a given value of E_0), while the squares (triangles) correspond to analysis which uses for evaluation (averaging) of the droplet's properties a PS whose semimajor and semiminor axes are 3/4 (1/2) of the lengths of the full PS used to describe the density distribution of the droplet. While the results using these different averaging volumes agree rather well, those that use a smaller averaging volume (scaling of the axes by 3/4 or 1/2) show less variation at smaller values of the field; the reason is that at smaller field values the shape fluctuations are larger, and they have a smaller effect on analyses that use reduced smaller averaging volumes (inscribed inside the droplet and thus less susceptible to fluctuations at the droplet's surface region).

As will be discussed below, the internal electric field strength is a function $E(E_0, \lambda)$ of both the external field (E_0) and the droplet's aspect ratio (λ). Values of the dielectric constant in Figure 3 calculated for applied fields below $E_0 \sim 0.5$ V/nm correspond to a much smaller range of internal fields ($E < 0.05$ V/nm); consequently, equilibration at such low values of E_0 is characterized by poorer statistics as regards the calculation of the dielectric constant. One observes in Figure 3 a pronounced hysteretic behavior of the dielectric constants that correlates with the corresponding hysteresis that characterizes the evolution of other physical properties of the droplet as a function of the applied field (see Figure 1), occurring as the droplet undergoes transitions between different states. The heavy curve in Figure 3 (between the two vertical dashed lines) corresponds to a fit (obtained through analysis of the MD results) of the dielectric constants to a theoretical curve (discussed below) that relates $\varepsilon(E)$ to the internal field (E), plotted versus the external field E_0.

To explore the predictions of the NLPS model, with its nonlinear dielectric saturation effects, we fit the observed dielectric constants $\varepsilon(E)$ (Figure 4) with an approximation that has been found useful[54,55] for the description of experimentally observed saturation effects, i.e.

$$\varepsilon(E) = n^2 + (\alpha/E)L(\beta E) \tag{5.4}$$

where $\alpha = a/s_1$; $a = \rho(n^2 + 2)\mu_0/(3\varepsilon_0)$; $\beta = s_2 b$; $b = (n^2 + 2)\mu_0/2k_BT$; n is the optical refractive index (n = 1 for the nonpolarizable formamide model used here); $\mu_0 \sim 0.08087$ e-nm (3.88 D) is the molecular dipole moment; $\rho \sim 14.7$ molecules/nm^3 is the liquid density; k_B is Boltzmann's constant; $T = 310$ K; and $L(x) = \coth(x) - 1/x$ is the Langevin function. We refer to eq 5.4 as the generalized Booth (or Booth−Onsager) equation, where we use the scaling parameters s_1 and s_2 (of order unity) as fitting parameters; in the theory developed in ref 54 these parameters take specific values (see below) which reduce eq 5.4 to previous treatments. While other (similar) functional forms[55] have been suggested, eq 5.4 has the merit of retaining the dependence of the dielectric constant on a host of material properties, and the values of s_1 and s_2 can serve as comparative measures of the dielectric response to that of other materials. The values $s_1 = s_2 = 1$ give the Booth−Onsager formula[54] for simple liquids with relatively small molecular dipole moments, while $s_1 = 73^{1/2}/7 \sim 1.22$ and $s_2 = 73^{1/2}/3 \sim 2.85$ give the Booth−Kirkwood formula[54] in which nearest-neighbor correlations due to hydrogen bonding (in water) are taken into account in performing ensemble averaging. Expressing the electric field in units of volts/nanometers and using the appropriate parameters for our system, we find

for the coefficients a and b (defining α and β in eq 5.4) the values $a = 21.5$ V/nm and $b = 4.53$ $(\text{V/nm})^{-1}$.

Because of the large variation in the results obtained in our simulations for internal fields less than 0.05 V/nm, we restrict ouselves to results corresponding to larger fields (i.e., $E > 0.05$ V/nm) in the fitting analysis. The solid curve in Figure 4 was obtained via the use of dielectric constants computed (as discussed above) in a smaller averaging volume of the PS (i.e., scaling the semiaxes by 3/4) and using eq 5.4 with $s_1 = 0.947$ and $s_2 = 1.117$; a similar result is obtained for analysis using 1/2 scaling of the PS semiaxes. It is of interest to note that eq 5.4 provides a remarkably good description of the simulation data with the values of the adjustable parameters s_1 and s_2 being close to unity; this corresponds to a parameter-free analysis that employed the density, dipole moment, and temperature obtained from the MD simulations

Some interesting features pertaining to the results displayed in Figures 3 and 4 merit further notice:

(i) For the low-field range, where elongation of the droplet is essentially insignificant (see Figure 1a before the shape transition), the internal electric field is much smaller than the corresponding external field. When the external field E_0 attains a value just exceeding the critical field (~0.5 V/nm), which leads to shape instability of the droplet (Figure 1a), many properties of the droplet vary in a rather marked manner (Figure 1), including the internal field E. Note also that in the transition region from liquid to crystalline droplet (see Figure 4, $E \sim 1.2$ V/nm) the curves corresponding to the liquid and ordered states display an overlap region and run (essentially) parallel to each other. Thus, in this region two different values may be obtained for the same internal field E: one for the liquid droplet and one for the droplet in the ordered state.

(ii) One of the more intriguing observations that we made concerns the finding that the droplet transforms from a liquid to a solid phase when the dielectric constant $\varepsilon(E)$ (decreasing in magnitude with increasing field E) just reaches the value $\varepsilon(E_{\text{liq-sol}}) \sim 18$ (see Figures 3 and 4). Indeed, in studies of the stability of dielectric drops in electric fields (with no saturation effects, see ref 5 for a review), it has been found that when the dielectric constant ε exceeds a value of about 18 one may obtain two distinct solutions for the drop shape having conical ends, while for $\varepsilon < 18$ only a single solution exists, having rounded drop ends. In the context of our study, we may conclude that when $\varepsilon(E)$ is above ~18 there are conditions involving interfacial stress balances that restrict the possible shape of the droplet near its ends. However, when the value of $\varepsilon(E)$ drops below ~18 these restrictions are relaxed and concomitantly crystalline order emerges. This suggests that the transition from a liquid droplet to one with crystalline symmetry, and the associated appearance of different boundary conditions and geometry, is inhibited by the development of interfacial stresses when the dielectric constant goes above $\varepsilon(E) \sim 18$, driving the droplet to geometries that are inconsistent with a nascent crystalline form, thus maintaining its liquid nature for $\varepsilon(E) > 18$.

It is important to note that the aforementioned relations between E_0, E, and $\varepsilon(E)$ may be used to write a defining relation for the electric field strength inside the droplet (E) as a unique function $E(E_0, \lambda)$ of the applied field, E_0, and aspect ratio, λ. Thus, with the expression for $\varepsilon(E)$ given in eqs 5.4 and 5.3a one can write (in dimensionless form) a determining relation for the field strength E in terms of E_0 and λ

$$x_0 = x + c(\lambda)L(x) \tag{5.5}$$

where $x_0 = s_2 bE_0$, $x = s_2 bE$, and $c(\lambda) = abn(\lambda)s_2/s_1$; the parameters (a,b,s_1,s_2) are defined following eq 5.4 (see above). We remark that the general form of the relation in eq 5.5 is $x_0 = [1 + (n^2 - 1)n(\lambda)]x + c(\lambda)L(x)$. In the above, we used the optical refractive index for our system, n = 1. For given E_0 and λ (or x_0 and λ), there is a unique solution, x, to eq 5.5, which may be easily found using a simple iterative method. Consequently, for analytical purposes, the internal field strength inside the droplet may be viewed as a given continuous function $E(E_0, \lambda)$ of the external field and the droplet aspect ratio.

B. Free Energy and Its Minimization. *Nonlinear Prolate Spheroidal (NLPS) Free-Energy Model.* When the dielectric constant of the fluid droplet is taken to be independent of the internal electric field, the total free energy in the prolate spheroid (PS) model, $F_{\text{PS}} = F_{\text{polz}} + F_{\text{surf}}$, consists of an electrical polarization term $F_{\text{polz}} = -1/2PE_0$ and a surface energy $F_{\text{surf}} = \gamma A$ (see, for example, ref 29), where A is the surface area of the PS, E_0 and E are the external and internal electric field along the z-axis; and P is the total dipole moment of the droplet along the z-axis (see eqs 5.1−5.3). When the dielectric constant is allowed to vary with the internal field strength, an additional term is necessary to obtain a free energy for the NLPS model

$$F_{\text{NLPS}} = -1/2PE_0 + \gamma A(\lambda) + \varepsilon_0 V/2 \int_0^{E(E_0,\lambda)} E^2 \varepsilon'(E)\mathrm{d}E \tag{5.6}$$

consistent with the general thermodynamic relation[51] (at constant temperature)

$$\mathrm{d}F = -P\mathrm{d}E_0 \tag{5.7}$$

For details of the derivation of eq 5.7, starting from eq 5.6, see the Appendix. The third term on the right-hand-side of eq 5.6 is denoted by F_{sat}. It is associated with saturation effects and is absent when the dielectric constant is independent of field strength. In eq 5.6, $\varepsilon'(E)$ is the derivative of ε with respect to the internal electric field, and the reference point of the free energy is the state with vanishing external field. The form of the free energy may be rewritten in various ways, having different interpretations. For example, one could replace $E^2\varepsilon'(E)$ in the integrand of F_{sat} by $E(\varepsilon_{\text{d}}(E) - \varepsilon(E))$ where the derivative of the displacement field $\varepsilon_{\text{d}} = (1/\varepsilon_0)\mathrm{d}D/\mathrm{d}E$ is the differential dielectric constant which has been found useful in the study of dielectric saturation phenomena.[55]

As discussed earlier, the electric field inside the droplet, E, may be considered as a well-defined function of E_0 and λ so that the dipole moment of the droplet P given in eq 5.3b may also be viewed as a function of E_0 and λ. The free energy in eq 5.6 is therefore a function of the applied external field, E_0, which can be viewed as an external control variable, and the droplet's aspect ratio, λ, which characterizes the droplet's response to the applied field as well as its state of thermodynamic equilibrium. In the differential $\mathrm{d}F = [\partial F_{\text{NLPS}}/\partial E_0]\mathrm{d}E_0 + [\partial F_{\text{NLPS}}/\partial\lambda]\mathrm{d}\lambda$, one finds from direct differentiation of eq 5.6 (see Appendix) that $\partial F_{\text{NLPS}}/\partial E_0 = -P$, while the second term is set to zero, $\partial F_{\text{NLPS}}/\partial\lambda = 0$, as this is the condition that the droplet responds to the applied field by a change in aspect ratio to minimize the free energy (also $\partial^2 F_{\text{NLPS}}/\partial\lambda^2 > 0$). In performing these differentiations, one uses the explicit functional dependence of the free energy on E_0 and λ,

e.g., eq 5.3b. In addition, it is interesting to note that the derivatives of the integral saturation term with respect to E_0 and λ, that is $(V\varepsilon_0/2)E^2\varepsilon'(E)\partial E(E_0, \lambda)/\partial E_0$ for E_0 (and a similar form for λ), cancel the additional identical terms arising from differentiation of the polarization term with respect to E_0 or λ when ε is a function of E. As a result of these cancellations, $\partial F_{NLPS}/\partial E_0$ and $\partial F_{NLPS}/\partial\lambda$ give the same functional form as when there is no saturation term, i.e., $\partial F_{NLPS}/\partial E_0 = -P$. Also, the condition $\partial F_{NLPS}/\partial\lambda = 0$ gives a relation between the derivatives (with respect to λ) of the depolarizing factor and the area, $n'(\lambda)P^2/(2\varepsilon_0 V) + \gamma A'(\lambda) = 0$, that holds true both in the original PS model as well as in the NLPS model where saturation effects are included. It is interesting to note here that the latter equation leads to a simple relation between the pressure inside the undistorted droplet, the droplet polarization, and some geometrical factors

$$\mathscr{P}/\varepsilon_0 = (3\Pi_0/\varepsilon_0)^{1/2} g(\lambda) \tag{5.8}$$

where $\mathscr{P} = P/V$ (see eq 5.1); $\Pi_0 = 2\gamma/R$ is the pressure inside the droplet of radius R at zero field; and $g(\lambda) = [-(A'(\lambda)/A_0)/n'(\lambda)]^{1/2} = [-d\tilde{A}/dn]^{1/2}$ with $A_0 = 4\pi R^2$ and $\tilde{A} = A(\lambda)/A_0$.

Using the expression for $\varepsilon(E)$ given in eq 5.4, one can evaluate the saturation integral term F_{sat} in the free-energy expression (eq 5.6). The result may be written as

$$F_{sat} = -1/2PES(x) \tag{5.9a}$$

$$S(x) = 2\ln[\sinh(x)/x]/[xL(x)] - 1 \tag{5.9b}$$

where ln [ ] is the natural logarithm and $x = s_2 bE$ (as in eq 5.5). The free energy $F_{NLPS} = F_{polz} + F_{surf} + F_{sat}$ can now be written as

$$F_{NLPS}(E_0, \lambda) = -1/2PE_0 + \gamma A(\lambda) - 1/2PES(x) \tag{5.10}$$

with the explicit reminder that all of the variables involved are functions of E_0 and λ. P is given in eq 5.3b in terms of E, $\varepsilon(E)$, and $n(\lambda)$. $\varepsilon(E)$ is given in eq 5.4, and $E(E_0, \lambda)$ is uniquely determined from eq 5.5. The saturation function $S(x)$ has the limits $S(0) = 0$ and $S(x) \rightarrow 1$ for large x, so that for large external (and associated internal) fields the new term in the free energy, F_{sat}, approaches $-1/2PE$. As we discussed earlier, the droplet may change phase in sufficiently high fields, and the above analysis will be modified.

Bond Number. In studies of fluid droplets interacting with external fields such as gravitational or electric fields, and possibly in the presence of surfaces where interfacial energies play a role, it is common to define dimensionless numbers, called Bond numbers, that characterize the ratio (and relative importance) of the various body forces to surface tension forces at the liquid interfaces. In studies of droplets in electric fields, an electric bond number $B_E = \varepsilon_0 E_0^2 R/\gamma$ is frequently used (where γ is the surface tension), expressing the ratio between the energy associated with electric polarization forces that tend to elongate the droplet and the surface energy associated with capillary forces that tend to contract the droplet; depending on the particular study, some variants of the above definition are sometime used. We will employ here the definition of B_E given above and normalize the energies to a dimensionless form by dividing them by the surface energy of the undeformed droplet: $F_{PS} \equiv F_{PS}/(4\pi R^2\gamma)$ and similarly for the components of the free-energy; for our system $4\pi R^2\gamma \sim 0.0119$ eV/molecule. We have[29,51]

$$F_{NLPS} = F_{polz} + F_{surf} + F_{sat} \tag{5.11a}$$

$$F_{polz} = -(B_E/6)(\varepsilon - 1)/\{1 + (\varepsilon - 1)n\} \tag{5.11b}$$

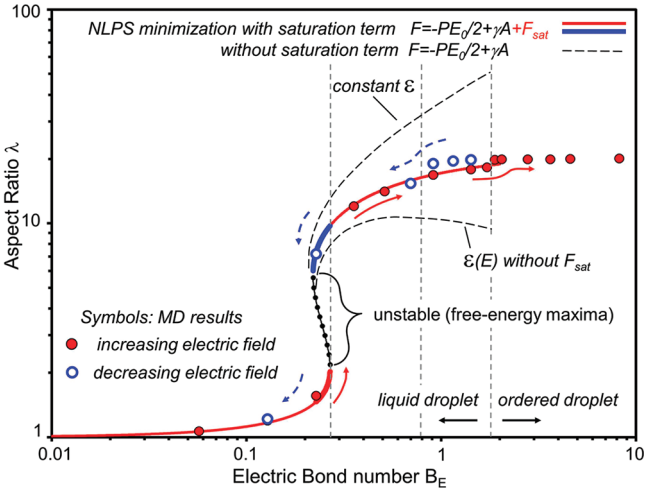

Figure 5. Variation of the droplet aspect ratio, λ, as a function of the electric Bond number, as predicted from minimization of the free energy with respect to λ (solid and dashed lines). Results from MD simulations are given by the dots, with the solid dots (red) obtained for increasing applied fields and the open ones (blue) for decreasing fields. The solid lines, which agree with the MD simulation results, were obtained through the use of the full expression for the free energy in the nonlinear prolate spheroidal model F_{NLPS} (see eqs 5.11(a−d)). The two dashed curves correspond to modified free-energy expressions: the lower one when the saturation term (F_{sat}) is omitted, and the upper one corresponds to the use of a constant field-independent dielectric constant. The first underestimates the MD results, and the second overestimates them. The thin solid lines (red) correspond to regions of the applied fields (and thus B_E values) where there is a unique shape (that is, a single value of λ) that minimizes the free energy. In the S-shaped region, associated with intermediate values of B_E, $0.220 \leq B_E \leq 0.269$, there are multiple solutions for each value of B_E, two minima (one, $F_{NLPS,1}$, lying on the lower branch of the S-curve, and the other, $F_{NLPS,2}$, lying on the upper branch) and one maximum (the latter is marked as a region of instability, denoted by a dotted line). When entering the S-shaped region from lower B_E values $F_{NLPS,1} < F_{NLPS,2}$, until for $B_E = 0.237$ the two minima take the same value, and for larger B_E values $F_{NLPS,1} > F_{NLPS,2}$. For sufficiently high bond number, the liquid droplet undergoes crystallization. Our NLPS model is valid up to the electrocrystallization point.

$$F_{surf} = (1/2)(1 - e^2)^{(1/3)}[1 + (\sin^{-1} e)/(e(1 - e^2)^{(1/2)})] \tag{5.11c}$$

$$F_{sat} = F_{polz}(E/E_0)S(x) \tag{5.11d}$$

We recall here that the eccentricity, e, is given by $e^2 = 1 - 1/\lambda$, where λ is the aspect ratio of the PS droplet.

For a given value of the external field E_0, the free energy F_{NLPS} is a function of the droplet shape through the aspect ratio λ, appearing in the eccentricity $e(\lambda)$ and internal electric field $E(E_0, \lambda)$, and it may exhibit one or more local minima or maxima with respect to variation of λ. The values of the aspect ratio λ associated with minima of F_{NLPS} define the stable (or metastable) droplet shapes.[29] We will perform the variation of the aspect ratio numerically to find the predicted stable configurations of the droplet for a wide range of external fields and compare a number of predictions from the above NLPS model which is based on continuum macroscopic theory, with results obtained from the MD simulations. Specifically, for a given applied field E_0 we assume an initial value of the aspect ratio

$\lambda = 1$ and vary λ in small increments ($\Delta\lambda = 0.01$), evaluating the free energy and recording the extremal points for each value of E_0. Key ingredients in this model are the new free-energy contribution F_{sat}, the function $\varepsilon(E)$ parametrized as described above using the MD simulation results, and the internal field strength $E(E_0, \lambda)$ which is obtained via eq 5.5 in the course of the incremental λ search for each external field E_0.

Droplet Shape versus Bond Number. The aspect ratios of the droplet deduced directly from the MD simulation data by means of axial and radial binning of the molecular number density (described earlier, see Section 4) are shown in Figure 5 (symbols) as a function of the electric bond number B_E. The aspect ratios that were found to minimize (through the numerical search procedure outlined above) the NLPS free energy (eqs 5.11a−d) for each value of E_0 are given by the solid curves. The regions associated with field strengths below $E_0 = 0.486$ V/nm ($B_E = 0.220$) [nearest MD simulated point at $E_0 = 0.5$ V/nm and $B_E = 0.228$] and above $E_0 = 0.538$ ($B_E = 0.269$) [nearest MD simulated point at $E_0 = 0.625$ V/nm and $B_E = 0.356$] are depicted by the curve segments colored red, and they correspond to the NLPS free energy, F_{NLPS}, having only one minimum with respect to the aspect ratio. For intermediate values of the Bond number, that is within the S-shaped region, $0.220 \leq B_E \leq 0.269$, the free energy, F_{NLPS}, has two minima: one lying on the lower branch, $F_{NLPS,1}$ (B_E, λ_1), and the other lying on the upper branch, $F_{NLPS,2}$ (B_E, λ_2), with $\lambda_1 < \lambda_2$ (represented, respectively, by the red and blue heavy line segments). In addition to the two minima, the free energy has also one maximum for each of the bond numbers associated with the S-shape interval, corresponding to shape instability of the droplet (represented by the middle black dotted segment); for a discussion on multiple solutions, see, for example, refs 5, 29, 33, and 57. When entering the S-shaped region from lower B_E values, $F_{NLPS,1} < F_{NLPS,2}$, until for $B_E = 0.237$ the two minima take the same value, and for larger B_E values $F_{NLPS,1} > F_{NLPS,2}$.

We call attention to the very good agreement that is found between the MD results and the predictions of the NLPS model developed here. In particular, note the MD point (blue open circle on the heavy blue curve at $B_E = 0.228$) that was obtained in the simulation by lowering the applied field from the previous stable configuration of the elongated droplet (open blue point on the red color curve at $B_E = 0.698$) into the S-shaped region.

It is of particular interest to assess the contribution of the saturation term in F_{NLPS} (eq 5.11d). The predicted aspect ratios obtained from the NLPS (and PS) model are shown in Figure 5 (upper dashed line) up to the point of droplet crystallization for a model where one takes the dielectric constant of the droplet to be independent of the strength of the field (that is, the common PS model) and equal to the zero field value $\varepsilon(E = 0) \sim 39.2$ (see ref 58). When the dielectric constant $\varepsilon(E)$ is allowed to vary, but the dielectric saturation term F_{sat} is not included in the free-energy minimization, the predicted aspect ratios vary as depicted by the lower dashed curve in Figure 5. From these results, we conclude that both the field-dependent dielectric constant and the saturation term are essential for a correct description of the field-induced droplet shape.

Comparison of Free Energies Calculated from MD and the NLPS Model. The free energy of the droplet under the influence of an applied field can be calculated in several ways. Besides the minimization of the NLPS model free energy described above, one may use the MD results and the basic relation in eq 5.7 to evaluate directly

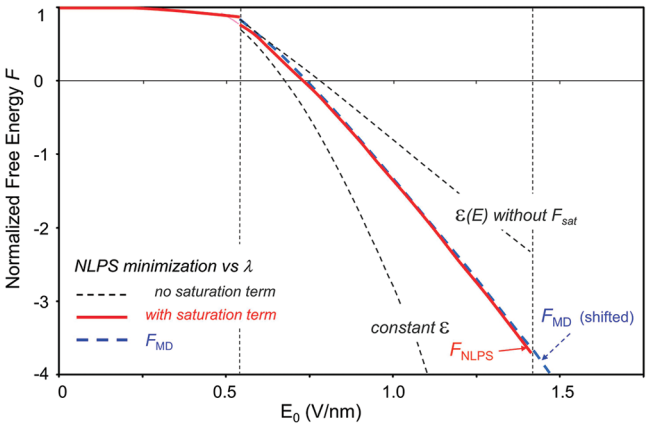

Figure 6. Comparison of the free energy F_{NLPS} (solid red curve) computed with the use of the minimization of the NLPS free energy with respect to the aspect ratio (for each value of E_0), with the free energy F_{MD} (blue dashed curve, marked as F_{MD} (shifted)) computed directly from integration of the droplet's dipole moments as obtained from the MD simulations. The two dashed curves show the predicted free energy for a constant and a variable dielectric constant when the free energy does not include the saturation term. The energies are normalized through division by the surface energy at zero field $F_{surf0} \equiv 4\pi R^2\gamma$ (~0.0119 eV/molecule), resulting in the normalized NLPS free energy F_{NLPS} being equal to unity at $E_0 = 0$.

$$F_{MD} = -\int_0^{E_0} P_{MD}(E_0)\,dE_0 \qquad (5.12)$$

where $P_{MD}(E_0)$ is a piecewise polynomial fit to the calculated dipole moments of the droplet (proportional to the data presented in Figure 1d). We present in Figure 6 the free energies obtained from both the MD results, F_{MD}, and the NLPS model, F_{NLPS}. The energies are normalized through division by the surface energy at zero field $F_{surf0} \equiv 4\pi R^2\gamma$ (~0.0119 eV/molecule), resulting in the normalized NLPS free energy F_{NLPS} being equal to unity at $E_0 = 0$. The normalized free energy, F_{MD}, from the integrated MD data does not include the zero field surface energy term, and therefore it is shifted upward by 1.0 for comparison with F_{NLPS}.

The free energy F_{MD} (eq 5.12), shown as a blue dashed line in Figure 6, is in remarkable agreement with the numerical minimization of the free energy F_{NLPS} (eqs 5.6, 5.10, and 5.11) based on the NLPS model. As for the aspect ratios (Figure 5), we show here also the predicted free energies (light dashed lines) obtained when a nonvarying dielectric constant is used, $\varepsilon = \varepsilon(E = 0)$, or when a nonconstant $\varepsilon(E)$ is employed but a saturation term is not included in the free-energy expression. Comparison of these results with the MD data and the full F_{NLPS} reaffirms our conclusion concerning the importance of including the term describing saturation effects in the free energy.

The individual contributions to the free energy, arising from the polarization, surface, and saturation terms, are displayed in Figure 7. We show the predictions of the NLPS model developed for a fluid droplet (that is up to the point of droplet crystallization) as solid colored lines. For the more general MD free energy (eq 5.12), we extend the integration into the ordered droplet region. The polarization, surface, and saturation terms based solely on the configuration of the droplet as given by the MD data (this does not involve any minimization) are depicted

dx.doi.org/10.1021/jp206673j | J. Phys. Chem. C 2011, 115, 20343–20358

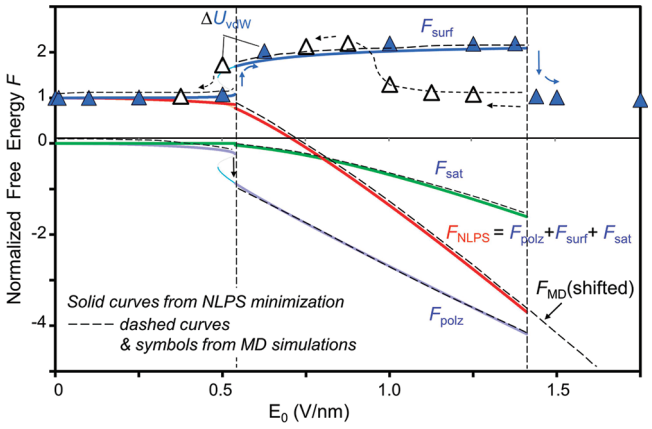

Figure 7. Polarization F_{polz} (solid thin blue line), surface F_{surf} (solid darker blue line), and saturation F_{sat} (solid green line) contributions to the total free energy F_{NLPS} (solid red line) computed through the minimization of the NLPS free energy (for each value of the external applied field, E_0), plotted versus the applied electric field. The light blue line continuations of F_{polz} and F_{surf} (to the left of the vertical dashed line at $E_0 = 0.55$ v/nm) correspond to the hysteresis obtained for the NLPS model when lowering the applied field from a state of an elongated droplet; these light blue lines connect to the corresponding solid blue curves (to the left of the vertical dashed line) through the instability region (see also Figure 5). The free energy obtained from the MD simulations (F_{MD}, see eq 5.12) and the corresponding contributions to it (computed by substituting the observed MD results into the expressions for the three terms of the NLPS free energy, with no minimization involved) are depicted by the respective dashed line. The very close agreement found for all of the terms between the MD results and the NLPS model predictions is evident. Also shown is the close correspondence between the relative variations in surface free energy and the observed relative variations in the vdW component of the internal energy. The triangles (filled for increasing E_0 and empty for decreasing field) give the MD calculated vdW contribution to the internal energy. The energies are normalized through division by the surface energy at zero field $F_{surf0} \equiv 4\pi R^2\gamma$ (~0.0119 eV/molecule), resulting in the normalized NLPS free energy F_{NLPS} being equal to unity at $E_0 = 0$.

by the dark dashed curves for the three components of the free energy in Figure 7, and they are found to be in very good agreement with those predicted by our model (shown by the solid curves).

It has been noted[51] that an increase in the permittivity of a medium (not involving shape and/or areal changes and not including dielectric saturation effects) results in a lowering of the free energy, and the reverse is true for a decrease in the medium's permittivity. On the other hand, in our case we observe that with increasing applied fields the free energy of the droplet takes lower values (more negative values, see Figure 6), although, as discussed above, we found a lowering of the dielectric constant (under the influence of the applied field) relative to its zero field value (Figures 3 and 4). This behavior is not contradictory, and it is a consequence of the finite size of our nanodroplet (i.e., the effect of the variable surface contribution in connection with the droplet's field-induced shape changes), as well as the influence of the saturation term. Indeed, for any given (nonzero) value of the applied field (E_0), we find (see Figure 6) that the free energy for a model with a constant dielectric permittivity ($\varepsilon \equiv \varepsilon(E = 0)$) is lower (more negative) than that calculated with a field-dependent $\varepsilon(E) < \varepsilon$. On the other hand, a model with a field-dependent dielectric permittivity, but without the inclusion of saturation effects, gives for any value of the applied field a free energy which is larger than the one where dielectric saturation is included (see Figure 6). We remark in closing this discussion that the effects of a varying dielectric constant also influence the polarization term F_{polz} of the free energy, and it is the minimization of the total free energy with respect to the aspect ratio, involving the interplay of all of the contributions to it, that determines the state of the droplet and its free energy.

van der Waals Contribution. An interesting relationship is found for the variations in the surface energy and the contributions to the droplet's potential energy arising from the van der Waals (vdW) component of the internal energy. The normalized surface energy is $\gamma A(\lambda)$ expressed in units of $\gamma A(\lambda = 1)$, where $A(\lambda)$ is the area of the prolate spheroidal droplet, and it is a function of the shape of the droplet only (eq 5.11c). The normalized surface energy was computed with the use of a polynomial fit to the values of the aspect ratio λ recorded in the MD simulation, and it is depicted by the upper dashed curve in Figure 7; the curve essentially overlaps the surface contribution (F_{surf}) to F_{NLPS}. The vdW contributions to the internal energy, averaged for each MD equilibration (also normalized by dividing by $4\pi R^2\gamma \sim$ 0.0119 eV/molecule and shifted to 1.0 to coincide with $F_{surf}(E_0 = 0)$) is shown in the upper part of Figure 7 (triangles). Up to the droplet crystallization point, we find close correspondence between the variations (from zero field) of the vdW internal energy contributions and the variations of the surface energy (even in the metastable region). Crystalline ordering of the droplet is accompanied by a drop of the vdW energy to its low-field value (i.e., $E_0 \leq 0.5$ V/nm).

For many materials, a close association is found between the surface energy and the vdW forces for many materials,[59] although the nature of the contributions to the surface energy becomes more complex for highly polar hydrogen-bonding liquids such as formamide.[59] Since the surface energy is correlated with the reduced coordination of molecules at the surface, it is rather natural that the changes in energy arising from the short-range intermolecular vdW interactions are closely related to the variations in the surface energy as the surface area and geometry undergo changes.

C. Entropy. To gain a better understanding of the driving forces underlying the field-induced structural variations of the droplet, we compute changes in the free energy and the entropy that are associated with the response of the droplet to the applied electric field. Taking the point of zero electric field as a reference, the changes in the Helmholtz free energy are given by $\Delta F = \Delta U - T\Delta S$, where ΔU and ΔS are, respectively, the changes in internal potential energy and entropy as the electric field E_0 is varied. The calculation of the free energy $\Delta F = \Delta F_{MD}$, through numerical integration of the polarization energy (eq 5.12), was described in the preceding section and is shown in Figure 8. Along with the free energy ΔF_{MD}, we display again in Figure 8 (dashed line) the free energy of the nonlinear prolate spheroid model, ΔF_{NLPS} (given relative to its value at zero field), as obtained from minimization of the prolate spheroid free energy. Comparison between ΔF_{MD} and ΔF_{NLPS} illustrates the remarkable agreement between the MD and analytical model results (note that, as before, the energies are scaled by the zero-field surface energy); the energy and entropy changes are plotted in Figure 8 relative to their values under field-free ($E_0 = 0$) conditions which are taken as reference.

The internal energy ΔU_{MD} shown in Figure 8 was obtained as a piecewise polynomial fit to the time-averaged potential energies

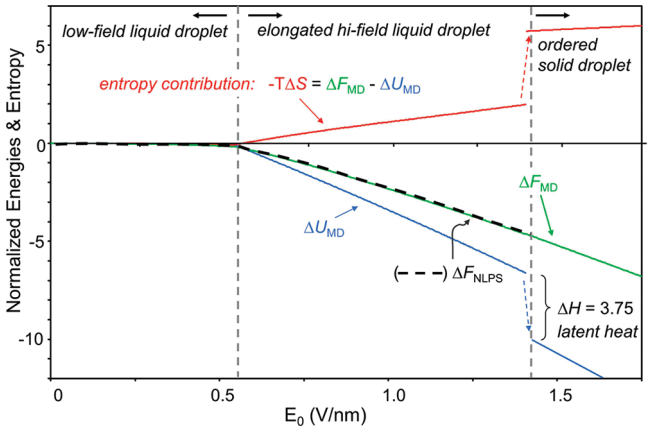

Figure 8. Entropic contribution ($-T\Delta S$, red line) to the free energy (ΔF_{MD}, green line) plotted as a function of the applied electric field. Also shown is the change in the internal potential energy, ΔU_{MD} (blue line), and the free energy calculated via the NLPS model (ΔF_{NLPS}, dashed black line). The entropy change and the energy changes are plotted relative to their values under field-free ($E_0 = 0$) conditions which are taken as reference. The energies are normalized through division by the surface energy at zero field $F_{surf0} \equiv 4\pi R^2\gamma$ (~0.0119 eV/molecule). The entropy increases ($-T\Delta S$ decreases) with increasing field for small droplet elongation and decreases for increasing fields after the droplet has become highly elongated. The entropy reaches a maximum in the region $E_0 \sim 0.5-0.6$ V/nm where the droplet undergoes a transition to a more highly elongated state (see Figure 1(a)). The calculated fusion enthalpy is $\Delta H = 0.045$ eV/molecule = 4.3 kJ/mol.

obtained from the MD equilibration for each applied field E_0. The marked drop in potential energy that occurs when the droplet orders corresponds to a latent heat (enthalpy of fusion) $\Delta H \sim 0.045$ eV/molecule or ~4.3 kJ/mol (the experimental[60] enthalpy of fusion for bulk formamide at 276 K is ~8 kJ/mol).

The entropic contribution to the free energy, $-T\Delta S = \Delta F - \Delta U$, is also shown in Figure 8. We find in the low-field region ($E_0 < 0.5$ V/nm) prior to elongation of the liquid droplet that $-T\Delta S$ and ΔU are both negative, with essentially the same magnitude, and the two become more negative as E_0 increases and approaches the point of shape instability ($E_0 \sim 0.55$ V/nm). The entropy therefore *increases* with field strength for small droplet elongations where the field may influence the molecular degrees of freedom only slightly. Subsequent to the sharp transition of the droplet to a more highly elongated state, the molecular dipoles become better aligned, and the entropic term $-T\Delta S$ changes sign. As seen from Figure 8, for higher applied fields, $-T\Delta S$ takes positive values (that is, ΔS takes negative values, corresponding to lowering of the entropy of the droplet as the field is increased further) and it makes a large contribution to the free energy. The entropy therefore reaches a maximum in the region $E_0 \sim 0.5-0.6$ V/nm where the droplet undergoes a transition to a more highly elongated state. Subsequently, the entropy decreases in a roughly linear manner with the increasing applied external field strength E_0, and the entropic component of the free-energy change, $-T\Delta S$, remains about a third the magnitude of the potential energy component ΔU up to the point of droplet crystallization. For the entropy of fusion of the droplet, we find $\Delta S/(310\ \mathrm{K}) \sim 14\ \mathrm{J/(mol\ K)}$; the experimental value[60] for bulk formamide is ~30 J/(mol K).We note that a depression in the enthalpy and the entropy of melting for nanoscale clusters is a current topic of experimental and theoretical interest.[61,62]

6. SUMMARY

Our investigations focused on characterization of the response of a neutral liquid dielectric droplet to applied uniform electric fields, on exploration and understanding of the molecular-scale origins of the behavior of the droplet and on formulation and testing of a proper continuum theory which would provide a faithful description of the field-dependent properties of the droplet. To these aims, we performed extensive constant-temperature molecular dynamics simulations of a formamide droplet with a 10 nm diameter, under field-free conditions, and when placed in electric fields of variable strengths. Analysis of the results obtained from the MD simulations formed the basis for the formulation of a theoretical model for the response of the droplet in terms of a nonlinear, field-dependent, dielectric permittivity and a continuum free energy expression, which were found to yield results in agreement with those obtained from our MD simulations.

To allow an efficient exploration of the equilibrium states of the formamide droplet (comprising 7150 molecules) for a wide range of applied electric fields (both of increasing and decreasing strength), we employed a fast multipole method (FMM), adapted to the elongated shape of the droplet under sufficiently high fields (see Section 2), which allowed long equilibration simulations with accurate and efficient evaluation of the electrostatic long-range intermolecular interactions. Prior to the investigation of the response of the dielectric droplet to applied fields, we have simulated and analyzed pertinent properties of field-free liquid formamide. The results that we obtained for the density, melting point, diffusion constant, and surface tension of the liquid compare well with the experimentally measured values, thus validating the simulation model.

Under the influence of an applied electric field, the initially spherical droplet was found to deform into a prolate spheroidal shape. Field-induced shape and crystallization transitions, found through molecular dynamics simulations, were described in Section 4. At a critical external field $E_{0c} \sim 0.50$ V/nm, these deformations culminate in a shape instability and a first-order shape transition to a slender liquid needle (see diffusion constant in Figure 1(b)) with an aspect ratio $\lambda = c/a = 12$ (Figures 1(a) and 2). In these elongated droplets, the molecular dipoles are found to be reoriented by the field along the long axis of the droplet (coinciding with the field direction), thus exhibiting a ferroelectric state (unlike the state of the droplet in field-free conditions).

For larger fields, further gradual enhancement of the dipole reorientation is observed (Figure 1(d)) leading to a first-order electro-crystallization transition[63] at $E_{0ec} = 1.4375$ V/nm. These processes are portrayed in increases in the positional order parameter (Figure 1(c)) and enhanced ordering of the molecular dipoles along the field direction (Figure 1(d)) and in accompanying decrease of the molecular diffusion (Figure 1(b)). Both transitions exhibit hysteresis as the change in the electric field is reversed. We note, in particular, the delayed remelting of the crystallized droplet (Figure 1(b)), occurring (in the course of decreasing the applied field) for $E_0 \sim 1.0$ V/nm.

From the results of the MD simulations, we have determined the field-dependent dielectric permittivity, $\varepsilon(E)$ (see eqs 5.1−5.3 and

symbols in Figures 3 and 4). An analytic continuum model for the dielectric permittivity of the droplet, which includes nonlinear contributions in the form of a field-dependent response and including dielectric saturation effects at high fields (see the generalized Booth equation, eq 5.4), was developed in Section 5.A. The model shows a decrease of the dielectric constant for increasing electric fields, and it was found to describe well the results of the MD simulations (Figures 3 and 4). We remark here on our observation that the droplet transforms from a liquid to a solid phase when the field-dependent dielectric constant reaches the value $\varepsilon(E_{\text{liq-sol}}) \sim 18$ (see Figures 3 and 4) correlating with previous observations (see review in ref 5).

This led us to develop an expression for the free energy of the droplet modeled as prolate spheroidal dielectric. The expression for the free energy of the nonlinear prolate spheroidal model, F_{NLPS}, includes polarization, surface, and saturation terms (eqs 5.6 and 5.10), and it may be expressed (eq 5.11) in terms of the electric Bond number, $B_E = \varepsilon_0 E_0^2 R/\gamma$. This allows us to evaluate the aspect ratios that minimize F_{NLPS} for the whole range of Bond numbers covered by the simulations. The results of such calculations plotted as λ vs B_E (Figure 5) exhibit an S-shaped curve, showing high and low Bond number regions where the minimization yields a unique aspect ratio (corresponding to a unique prolate spheroidal shape), and an intermediate Bond number interval where multiple solutions are found (that is, two λ values corresponding to free-energy minima and one λ corresponding to a free-energy maximum). These results obtained from the NLPS model for the total free energy, as well as the contributions of the polarization, surface, and saturation terms (Figures 6 and 7), agree with those obtained from the MD simulations, evaluated via an integral of the dipole moment of the droplet along the applied field direction (see eq 5.12). In all of the above, proper inclusion of saturation effects in the continuum description of the droplet free energy, expressed in terms of an electric field-dependent dielectric permittivity, is found to play an important role.

Subsequently, we included a brief discussion of the variation of the van der Waals intermolecular interaction energy (calculated in the course of the MD simulations), which, as a function of the applied field, was found to vary in a manner similar to the surface energy contribution, F_{surf}, of the NLPS continuum model F_{NLPS} (see Figure 7). We concluded with an analysis of the entropy variation with the applied field, showing that after the shape transition (i.e., for $E_0 > E_{0c}$) the elongation of the droplet, entailing preferential orientation of the molecular dipoles along the field directions (and crystalline ordering for larger fields), is associated with a decrease in the entropy (i.e., $-T\Delta S > 0$) (see Figure 8).

APPENDIX

In this appendix we provide details of the derivation of eq 5.7

$$dF = -P dE_0 \tag{A.1}$$

for the NLPS model from direct differentiation of the integrated form of this (see eq 5.6)

$$F_{\text{NLPS}} = -\frac{1}{2}PE_0 + \gamma A(\lambda) + \frac{1}{2}\varepsilon_0 V \int_0^{E(E_0,\lambda)} E^2 \varepsilon'(E) dE \tag{A.2}$$

Defining polarization, surface, and saturation components (F_{polz}, F_{surf}, and F_{sat}, respectively), the free energy can be written as

$$F_{\text{NLPS}} = F_{\text{polz}} + F_{\text{surf}} + F_{\text{sat}} \tag{A.3}$$

The differential of eq A.3 is

$$dF_{\text{NLPS}} = [\partial F_{\text{NLPS}}/\partial E_0] dE_0 + [\partial F_{\text{NLPS}}/\partial \lambda] d\lambda \tag{A.4}$$

We focus now on the first component of dF_{NLPS}; the second component involving λ is set to zero, since it is the condition for extremum (minimum) of F_{NLPS}. The polarization term, F_{polz}, of F_{NLPS} may be written (using the expression for P given by eq 5.3b)

$$F_{\text{polz}} = -\frac{1}{2}PE_0 = -\frac{1}{2}[\varepsilon_0 V(\varepsilon(E) - 1)/\{1 + (\varepsilon(E) - 1)n(\lambda)\}E_0]E_0 \tag{A.5}$$

The differential of F_{polz} is

$$dF_{\text{polz}} = \{\partial F_{\text{polz}}/\partial E_0(\text{explicit } E_0) + [\partial F_{\text{polz}}/\partial \varepsilon]\varepsilon'(E)[\partial E/\partial E_0]\} dE_0 \tag{A.6}$$

The derivative of the first term, involving the explicit appearance of E_0, gives

$$dF_{\text{polz}}(\text{explicit } E_0) = -P dE_0 \tag{A.7}$$

This is already the sole component of the total differential of the free energy A.1 (also eq 5.7), and thus the remaining contributions are expected to sum to zero.

The second term of dF_{polz} (eq A.6) involving the implicit appearance of E_0 (see eqs A.5 and A.6) gives

$$dF_{\text{polz}}(\text{implicit } E_0) = \frac{1}{2}\varepsilon_0 V {E_0}^2[-1/N + (\varepsilon(E) - 1)n(\lambda)/N^2]\varepsilon'(E)[\partial E/\partial E_0]\} dE_0 \tag{A.8}$$

where we have defined $N = 1 + (\varepsilon(E) - 1)n(\lambda)$. This can be simplified to

$$dF_{\text{polz}}(\text{implicit } E_0) = -\frac{1}{2}(\varepsilon_0 V {E_0}^2/N^2)\varepsilon'(E)[\partial E/\partial E_0] dE_0 \tag{A.9}$$

Using eq 5.3a, written as $E = E_0/N$, gives

$$dF_{\text{polz}}(\text{implicit } E_0) = -\frac{1}{2}\varepsilon_0 V E^2 \varepsilon'(E)[\partial E/\partial E_0] dE_0 \tag{A.10}$$

as the second polarization contribution (the first is eq A.7) to dF_{NLPS} (eq A.4).

The saturation component of F_{NLPS} (see eq A.2) is

$$F_{\text{sat}} = \frac{1}{2}\varepsilon_0 V \int_0^{E(E_0,\lambda)} E^2 \varepsilon'(E) dE \tag{A.11}$$

and its differential is

$$dF_{\text{sat}} = \frac{1}{2}\varepsilon_0 V E^2 \varepsilon'(E)[\partial E/\partial E_0] dE_0 \tag{A.12}$$

being the sole saturation contribution to dF_{NLPS} (see eq A.4).

The three contributions to dF_{NLPS} are given by eqs A.7, A.10, and A.12 which are to be summed to give the complete expression for dF_{NLPS} (eq A.4). Note that the contributions dF_{polz} (implicit E_0) (see eq A.10) and dF_{sat} (eq A.12) to dF_{NLPS} cancel

each other with the result that dF_{NLPS} is given by the same expression (see eq A.1)

$$dF_{NLPS} = -PdE_0 \quad (A.13)$$

as in the PS model which assumes the dielectric constant ε to be literally constant as opposed to the NLPS model where it is a function, $\varepsilon(E)$, of the electric field strength.

AUTHOR INFORMATION

Corresponding Author
*E-mail: uzi.landman@physics.gatech.edu.

BIOGRAPHIES

W. D. Luedtke is a Senior Research Scientist in the School of Physics at the Georgia Institute of Technology and a member of its Center for Computational Materials Science. He received his undergraduate degrees in Physics and Applied Mathematics in 1976 and his Ph.D. degree in Physics in 1984 from Georgia Tech. His research interests focus on studies of novel material behavior at the nanometer scale.

Jianping Gao received his B.Sc. from Zhejiang University in Hangzhou, China, and his Ph.D. in Physics (1989) from Brown University. He is currently a Senior Research Scientist in the Center for Computational Materials Science in the Georgia Tech School of Physics. His scientific interests include properties of nanoconfined fluids, nanotribology, complex molecular systems, and the development of computational methods.

Uzi Landman was born in Israel and received his B.Sc. from the Hebrew University in Jerusalem, M.Sc. from the Weizmann Institute of Science, and D.Sc. from the Israel Institute of Technology (Technion) (1969). In 1977 he joined the Georgia Tech School of Physics, where he is a Callaway Chair, Director of the Center for Computational Materials Science, and a Regents' and Institute Professor of Physics. He has authored over 400 articles in the areas of condensed matter theory, clusters, nanoscience, nanotribology, nanowires, self-assembly, microscopic hydrodynamics, transport and damage mechanisms in DNA, nanocatalysis, quantum dots, and strongly correlated electron systems, with a focus on the development and application of classical and first-principles quantum computational methodologies.

ACKNOWLEDGMENT

This research has been supported by Grant FA9550-08-1-0323 from the Air Force Office of Scientific Research. Computations were performed at the National Energy Research Scientific Computing Center (NERSC), Lawrence Berkeley National Laboratory, Berkeley, California.

REFERENCES

(1) Fenn, J. B. *Angew. Chem., Int. Ed.* **2003**, *42*, 3871–3894.
(2) Luedtke, W. D.; Landman, U.; Chiu, Y. H.; Levandier, D. J.; Dressler, R. A.; Sok, S.; Gordon, M. S. *J. Phys. Chem. A* **2008**, *112*, 9628–9649.
(3) Eggers, J. *Rev. Mod. Phys.* **1997**, *69*, 865–929.
(4) J. Eggers, J.; E. Villermaux, E. *Rep. Prog. Phys.* **2008**, *71*, 036601–036679.
(5) Stone, H. A.; J. R. Lister, J. R.; M. P. Brenner, M. P. *Proc. R. Soc. London A* **1999**, *455*, 329–347.
(6) Basaran, O. A.; L. E. Scriven, L. E. *Phys. Fluids A* **1989**, *1*, 799–809.
(7) Fernandez de la Mora, J. *Annu. Rev. Fluid Mech.* **2007**, *39*, 217–243.
(8) Saville, D. A. *Annu. Rev. Fluid Mech.* **1997**, *29*, 27–64.
(9) Moseler, M.; Landman, U. *Science* **2000**, *289*, 1165–1169.
(10) Bailey, A. G. *Electrostatic Spraying of Liquids*; Wiley: New York, 1988.
(11) Michelson, D. *Electrostatic Atomization*; Adam Hilger: Bristol, 1990.
(12) See articles in: *J. Aerosol. Sci.* **1994**, *25* (6), Special Issue on "Electrosprays: Theory and Applications".
(13) Grimm, R. L.; Beauchamp, J. L. *J. Phys. Chem. B* **2003**, *107*, 14161–14163.
(14) Saunders, C. P. R. In *Proceedings of the International Colloquium on Drops and Bubbles*; Collin, D. J., Plesent, M. S., Saffren, M., Eds.; Jet Propulsion Laboratory: Pasadena, CA, 1974.
(15) Duft, D.; Achtzehn, T.; Muller, R.; Huber, B. A.; Leisner, T. *Nature (London)* **2003**, *421*, 128–128.

(16) Huberman, M. N.; Rosen, S. G. *J. Spacecr.* **1974**, *11*, 475–480.
(17) Gamero-Castaño, M.; Hruby, V. *J. Propul. Power* **2001**, *17*, 977–987.
(18) Kenyon, R. W. *Chemistry and Technology of Printing and Imaging Systems*; Gregory, P., Ed.; Springer: London, 1996; pp 113−138.
(19) (a) Reneker, D. H.; Chun, I. *Nanotechnology* **1996**, *7*, 216–223. (b) Dzenis, Y. *Science* **2004**, *304*, 1917–1919.
(20) Loscertales, I. G.; Barrero, A.; Guerrero, I.; Cortijo, R.; Marquez, M.; Canan-Calvo, A. *Science* **2002**, *295*, 1695–1698.
(21) Tang, K.; Gomez, A. *J. Aerosol. Sci.* **1994**, *25*, 1237–1249.
(22) Naidu, M. S.; Kamarju, V. *High Voltage Engineering*; Tata McGraw-Hill: New Delhi, 2009. For recent work on the anisotropic spinoidal decomposition of a model polar dielectric medium in a strong electric field, see: Karpov, D. I.; Kupershtokh, A. L. *Tech Phys. Lett.* **2009**, *35*, 479–482 and papers cited therein.
(23) Rayleigh, Lord *Proc. R. Soc. London A* **1879**, *28*, 406–409.
(24) Rayleigh, Lord *Philos. Mag.* **1882**, *14*, 184–186.
(25) Zeleny, J. *Phys. Rev.* **1914**, *3*, 69–91.*Phys. Rev.* **1917**, *10*, 1-6.
(26) Wilson, C. T. R.; Taylor, G. I. *Proc. Camb. Phil. Soc.* **1925**, *22*, 728–730.
(27) Taylor, G. I. *Proc. R. Soc. London* **1964**, *A 280*, 383–397.
(28) Taylor, G. I. *Proc. R. Soc. London* **1969**, *A 291*, 159–166.
(29) Sherwood, J. D. *J. Fluid Mech.* **1988**, *188*, 133–146. We remark that the electrical polarization energy in this paper appears to contain several typos. We also note that the definition of electric bond number here is a factor of two larger than the definition used by Lister et al. in ref 5.
(30) Sherwood, J. D. *J. Phys. A: Math. Gen.* **1991**, *24*, 4047–4053.
(31) Wohlhuter, F. K.; Basaran, O. A. *J. Magn. Magn. Mater.* **1993**, *122*, 259–263.
(32) Li, H.; Halsey, H.; Lobkovsky, A. *Europhys. Lett.* **1994**, *27*, 575–580.
(33) Bacri, J. C.; Salin, D. *J. Phys. Lett.* **1982**, *43*, L649–L654.*ibid.* **1983**, *44*, L415−L420.
(34) (a) Kang, W.; Landman, U. *Phys. Rev. Lett.* **2007**, *98*, 064504-1–064504-4. (b) Kang, W.; Landman, U.; Glezer, A. *Appl. Phys. Lett.* **2008**, *93*, 123116-1–123116-3.
(35) Gamero-Castano, M.; Fernandez de la Mora, J. *J. Chem. Phys.* **2000**, *113*, 815–832.
(36) Loscertales, I. G.; Fernandez de la Mora, J. *J. Chem. Phys.* **1995**, *103*, 5041–5060.
(37) (a) Allen, M. P.; Tildesley, D. J. *Computer Simulation of Liquids*; Clarendon: Oxford, 1987. (b) Svanberg, M. *Mol. Phys.* **1997**, *92*, 1085–1088.
(38) Stevens, E. D. *Acta Crystallogr.* **1978**, *B34*, 544–551.
(39) Cornell, W. D.; Cieplak, P.; Bayly, C. I.; Gould, I. R.; Merz, K. M.; Ferguson, D. M.; Spellmeyer, D. C.; Fox, T.; Caldwell, J. W.; Kollman, P. A. *J. Am. Chem. Soc.* **1995**, *117*, 5179–5197. www.amber.ucsf.edu/amber/ff94/parm.dat
(40) Sigfridsson, E.; Ryde, U. *J. Comput. Chem.* **1998**, *19*, 377–395.
(41) Applequist, J.; Carl, J . R.; Fung, K.-K. *J. Am. Chem. Soc.* **1972**, *94*, 2952–2960.
(42) Perera, L.; Essmann, U.; Berkowitz, M. L. *J. Chem. Phys.* **1995**, *102*, 450–456.
(43) Greengard, L. F. *The Rapid Evaluation of Potential Fields in Particle Systems*; The MIT Press: Boston, 1988.
(44) Berendsen, H. J. C.; Postma, J. P. M.; van Gunsteren, W. F.; DiNola, A.; Haak, J. R. *J. Chem. Phys.* **1984**, *81*, 3684–3690.
(45) (a) Ladell, J.; Post, B. *Acta Crystallogr.* **1954**, *7*, 559–564. (b) Torrie, B. H.; Odonovan, C. O.; Powell, B. M. *Mol. Phys.* **1994**, *82*, 643–649.
(46) (a) Barnett, R. N.; Landman, U. *Phys. Rev. B* **1991**, *44*, 3226–3239.(b) Lide, D. R., Ed. *CRC Handbook of Chemistry and Physics*, 85th ed.; CRC Press: New York, 2004.
(47) Sagarik, K. P.; Ahlrichs, R. J. *Chem. Phys.* **1987**, *86*, 5117–5126.
(48) (a) Kirkwood, J. G.; Buff, F. P. *J. Chem. Phys.* **1949**, *17*, 338–343. (b) Frenkel, D.; Smit, B. *Understanding Molecular Simulations*, 2nd ed.; Academic Press: London, 2002; p 472.
(49) Landman, U.; Cleveland, C. L.; Brown, C. S. *Phys. Rev. Lett.* **1980**, *45*, 2032–2035.
(50) Lines, M. E.; Glass, A. M. *Principles and Applications of Ferroelectrics and related Materials*; Clarendon Press: Oxford, 1977.
(51) Landau, L. D.; Lifshitz, E. M. *Electrodynamics of Continuous Media*; Pergamon: New York, 1960.
(52) Stratton, J. A. *Electromagnetic Theory*; McGraw-Hill: New York, 1941.
(53) Powles, J. G.; Williams, M. L.; Evans, W. A. B. *J. Phys. C: Solid State Phys.* **1988**, *21*, 1639–1659.
(54) Booth, F. *J. Chem. Phys.* **1951**, *19*, 391–394. *ibid.* **1951**, *19*, 1327−1328. *ibid*. **1951**, *19*, 1615−1615.
(55) Liszi, J.; Meszaros, L.; Ruff, I. *J. Chem. Phys.* **1981**, *74*, 6896–6901. The first experiments on nonlinear dielectric effects recorded in 1920 a decrease of the electric permittivity of diethyl ether, showing a quadratic dependence on the field. See:Herweg, J. *Z. Phys.* **1920**, *3*, 36–47. As the subject developed, these effects became known as dielectric saturation effects. In the case of water, the decrease in the value of the dielectric permittivity was seen already over 70 years ago:Malsch, J. *Z. Phys.* **1928**, *29*, 770–777. More precise measurements showing that the decrease in value is proportional to the square of the electric field were made in 1975:Kolodziej, H. A.; Jones, B. P. *J. Chem. Soc., Faraday Trans. 2* **1975**, *71*, 269–274. Early theoretical models of nonlinear dielectric phenomena were based on phenomenological theories of dielectric continua. See:Debye, P. *Z. Phys.* **1935**, *36*, 100–101. Debye, P. *Z. Phys.* **1935**, *36*, 193–194. Onsager, L. *J. Am. Chem. Soc.* **1936**, *58*, 1486–1493. Kirkwood, J. G. *J. Chem. Phys.* **1939**, *7*, 911–919. A phenomenological equation has been proposed by Booth (see ref 54 and Fulton, R. L. *J. Chem. Phys.* **2009**, *130*, 204503-1–204503-10 and references therein). It was found to agree with results obtained for bulk water through MD simulations showing saturation effects (decrease of the dielectric permittivity with increasing field strength). See:Yeh, I. −C.; Berkowitz, M. L. *J. Chem. Phys.* **1999**, *110*, 7935–7042. More recent theoretical work on nonlinear effects in dipolar fluids focuses on microscopic approaches. See: Szalai, I.; Nagy, S.; Dietrich, S. *J. Chem. Phys.* **2009**, *131*, 154905-1–154905-9 and references cited therein.
(56) Frohlich, H. *Theory of Dielectrics*; Oxford University Press: New York, 1949.
(57) Miksis, M. J. *Phys. Fluids* **1981**, *24*, 1967–1972.
(58) The zero-field dielectric constant that we find for liquid formamide (∼39.2) is lower than the experimental value of ∼111. It has been noted by Essex, J. W.; Jorgensen, W. L. *J. Phys. Chem.* **1995**, *99*, 17956–17962 that fixed charge models tend to underestimate the dielectric constant. For a study such as ours, it is important to use the material constants determined specifically for the model fluid being used in developing ideas and theoretical models in a consistent manner.
(59) Israelachvili, J. N. *Intermolecular and Surface Forces*; Academic Press: London, 1991.
(60) NIST Chemistry WebBook, http://webbook.nist.gov/chemistry.
(61) Schmidt, M; Kusche, R.; Issendorff, B.v.; Haberland, H. *Nature* **1998**, *393*, 238–240.
(62) Jiang, Q.; Yang, C. C.; Li, J. C. *Mater. Lett.* **2002**, *56*, 1019–1021.
(63) The effect of electric fields on phase transformations of liquids (in particular electro-freezing of water) has been the subject of numerous experimental and theoretical investigations; for a most recent study, and references to earlier work, see: Stan, C. A.; Tang, S. K. Y.; Bishop, K. J. M.; Whitesides, G. M. *J. Phys. Chem. B* **2011**, *115*, 1089–1097. As discussed by Stan et al., previous experimental work (see refs 9−21 cited in the above reference) about the effect of electric fields on the freezing of water used systems in which freezing was initiated by the heterogeneous nucleation of ice and has provided inconclusive evidence that electric fields affect the homogeneous nucleation of ice. In the above paper, Stan et al. did not observe any effect of applied fields up to 1.6×10^5 V/m on the homogeneous nucleation in supercooled water droplets (as small as 70 μm in diameter) immersed in a perfluorinated liquid using a parallel-plate capacitor. Theoretical MD simulations on homogeneous systems showed field-induced freezing for fields around 5 V/nm (starting with Svishchev, I. M.; Kusalik, P. G. *Phys. Rev. Lett.* **1994**, *73*, 975–978). Other simulation studies, which focused on confined water films, showed formation of ice for fields of similar magnitude (see review by Zangi, R. *J. Phys.: Condens. Matter* **2004**, *16*, S5371–S5388). To date, MD simulations of only small water clusters (16 to 64 molecules, with temperatures of up to 240 K) have been performed, finding field-induced structural changes. See:Vegiri, A. *J. Mol. Liq.* **2004**, *110*, 155–168. Vegiri, A. *J. Chem. Phys.* **2002**, *116*, 8786–8798 and references therein.